A COMPUTATIONAL STUDY OF COLLISIONS RELEVANT TO CYANOGEN, CARBON DIOXIDE AND HELIUM IN ASTROPHYSICAL ENVIRONMENTS

by

WESAM HASAN EL-QADI

(Under the Direction of Phillip C. Stancil)

ABSTRACT

Collisions are very important in determining the abundances of the different species that exist in our world. Atoms, molecules, ions, electrons and even photons, have their concentrations dictated by the collisions they undergo. In this work, three types of collisions are studied. The photodissociation, collision with photons, of cyanogen (CN) is studied in chapter 1. Cross sections were computed for the $^2\Sigma^+(4) \leftarrow \mathrm{X}\ ^2\Sigma^+$, $^2\Sigma^+(5) \leftarrow \mathrm{X}\ ^2\Sigma^+$, $^2\Pi(4) \leftarrow \mathrm{X}\ ^2\Sigma^+$, and $^2\Pi(5) \leftarrow \mathrm{X}\ ^2\Sigma^+$ electronic transitions. Partial and LTE cross sections were evaluated for all rovibrational levels $(v''N'')$ of the ground electronic state of CN, X $^2\Sigma^+$, and over a large wavelength range of astrophysical interest. The results will allow for the calculation of reliable CN photodissociation rates for astrophysical environments with varying radiation and dust properties. The rotational quenching of CO_2 by collisions with He is the subject of Chapters 3 and 4. CO_2 was treated as a rigid rotor in the ground state. If CO_2 is initially in the rotational state specified by the rotational quantum number j_o, cross sections for transitions to all possible lower$-j$ rotational states, for a wide range of relative collision energy, were calculated. In Chapter 4, the emphasis is on rotational quenching of CO_2 by collisions with He in the ultracold regime. Complex scattering lengths and elastic and inelastic rotational quenching cross sections have been computed for carbon dioxide, with rotational excitation j as high as 200, due to ultracold ^{4}He collisions. It is predicted that the ratio of the elastic to inelastic cross section, or figure-of-merit, is sufficiently large that highly rotationally excited CO_2 could be a viable candidate for cooling and trapping. In chapter 5, new potential energy curves were used to calculate the cross section for excitation transfer from the He(2^3S) atoms to the He(1^1S) gas, the diffusion of He(2^3S) atoms in He(1^1S) gas, and the total elastic cross sections for the collision of He(1^1S) and He(2^3S) atoms. The results were compared to published results and a good agreement is observed. The elastic cross sections for the collision of He(1^1S) and He(3^3S) were calculated for the first time.

INDEX WORDS: Born-Oppenheimer approximation, adiabatic basis, diabatic basis, multichannel equations, close-coupling equations, coupled states approximation, scattering, photodissociation, scattering amplitude, scattering matrix, scattering cross sections, rigid rotor, rotational relaxation, CN, CO_2, He

A COMPUTATIONAL STUDY OF COLLISIONS RELEVANT TO CYANOGEN, CARBON DIOXIDE AND HELIUM IN ASTROPHYSICAL ENVIRONMENTS

by

WESAM HASAN EL-QADI

B.Sc., alQuds University, 1994
M.Sc., Bowling Green State University, 2000

A Dissertation Submitted to the Graduate Faculty
of The University of Georgia in Partial Fulfillment
of the
Requirements for the Degree

DOCTOR OF PHILOSOPHY

ATHENS, GEORGIA

2012

A Computational Study of Collisions Relevant to Cyanogen, Carbon Dioxide and Helium in Astrophysical Environments

by

Wesam Hasan El-Qadi

Approved:

Major Professor:	Phillip C. Stancil
Committee:	Wesley Allen Henning Meyer Susanne Ullrich

Electronic Version Approved:

Maureen Grasso
Dean of the Graduate School
The University of Georgia
December 2012

A Computational Study of Collisions Relevant to Cyanogen, Carbon Dioxide and Helium in Astrophysical Environments

Wesam Hasan El-Qadi

December 12, 2012

Acknowledgments

I would like to thank my advisor, Phillip C. Stancil, for his support and patience throughout my graduate work with him. I would also like to thank Benhui Yang for his help with the work related to CO_2. Also, the help of Robert C. Forrey and Naduvalath Balakrishnan. I would also like to thank Robert J. Buenker and Heinz-Peter Liebermann for providing the He-He potential interaction.

Contents

List of Figures **vii**

List of Tables **x**

1 Introduction **1**

1.1 Potential Energy Surfaces and the Born-Oppenheimer Approximation 2

1.2 Adiabatic vs. Diabatic Representation and the Multichannel Equations . . . 5

1.3 Scattering: a General Review 8

1.4 Photodissociation 11

1.5 Molecules in the Interstellar Medium 14

2 Photodissociation of Cyanogen **16**

2.1 Photodissociation Cross Sections 17

2.2 Potential Energy and Dipole Transition Moment Functions 18

2.3 Results and Discussion 20

2.4 Astrophysical Applications 27

3 Rotational Relaxation of Carbon Dioxide by Collisions with Helium Atoms **33**

3.1 The Multichannel and the Close-coupled Equations 35

3.2 The Cross Section for Rotational Transitions of a Rigid Rotor 41

3.3 Calculating the Cross Sections 43

3.4 Results: Cross Sections and Rate Coefficients 45

4 Quenching of Rotationally Excited CO_2 at Ultra Cold Temperatures 53

4.1 Introduction 53

4.2 The Complex Scattering Length 54

4.3 Results and Discussion 55

5 Dynamics of Excited Helium Scattering by Helium 64

5.1 Introduction 64

5.2 Collisions between Metastable Helium Atoms and Normal Helium Atoms . . 65

5.3 Cross-sections Results 71

6 Conclusions 75

References 78

List of Figures

2.1 Potential energy curves for the low-lying doublet electronic states of CN considered in this work which are dipole-connected to the X $^2\Sigma^+$ ground state. The notation follows that of [1]. 22

2.2 CN photodissociation partial cross sections as a function of wavelength . . . 23

2.3 CN photodissociation partial cross sections as a function of wavelength for the transition $^2\Sigma^+(5) \leftarrow$ X $^2\Sigma^+$ from two vibrational levels with different rotational quantum number N'' of the ground electronic state. (a) $v'' = 0$. (b) $v'' = 20$. 24

2.4 CN photodissociation partial cross sections as a function of wavelength for the transition $^2\Pi(5) \leftarrow$ X $^2\Sigma^+$ from two vibrational levels with different rotational quantum number N'' of the ground electronic state. (a) $v'' = 0$. (b) $v'' = 20$. 25

2.5 CN photodissociation partial cross sections as a function of wavelength for the transition from different vibrational levels v'' with the rotational quantum number $N'' = 0$ of the ground electronic state. (a) $^2\Sigma^+(5) \leftarrow$ X $^2\Sigma^+$. (b) $^2\Pi(5) \leftarrow$ X $^2\Sigma^+$. 26

2.6 CN LTE photodissociation cross sections as a function of wavelength for the transitions $^2\Sigma^+(4) \leftarrow$ X $^2\Sigma^+$, $^2\Sigma^+(5) \leftarrow$ X $^2\Sigma^+$, $^2\Pi(4) \leftarrow$ X $^2\Sigma^+$, and $^2\Pi(5) \leftarrow$ X $^2\Sigma^+$. (a) 500 K. (b) 3000 K. The dotted curves are for blackbody radiation at the indicated radiation temperatures. 31

3.1 Space-fixed, SF, coordinate system for the collision between a He atom and the CO_2 rigid rotor. 35

3.2 CO_2 quenching, from j=10 to all possible j', due to collisions with He. Top: State-to-state cross sections. Bottom: State-to-state rate coefficients as a function of temperature. 47

3.3 CO_2 quenching, from j=20 to all possible j', due to collisions with He. Top: State-to-state cross sections. Bottom: State-to-state rate coefficients as a function of temperature. 48

3.4 CO_2 quenching, from j=30 to all possible j', due to collisions with He. Top: State-to-state cross sections. Bottom: State-to-state rate coefficients as a function of temperature. 49

3.5 CO_2 quenching, from j=40 to all possible j', due to collisions with He. Top: State-to-state cross sections. Bottom: State-to-state rate coefficients as a function of temperature. 50

3.6 CO_2 Total rate coefficients for quenching from j =10, 20, 30, and 40 due to collisions with He as a function of temperature. 51

4.1 Real and imaginary parts, α and β, respectively, of the scattering length as a function of the rotational level j. All calculations were performed at 10^{-6} cm^{-1}. 56

4.2 Ratio of the imaginary part β to the real part α of the scattering length for ^{4}He collisions with CO_2 as a function of the rotational level j. All calculations were performed at 10^{-6} cm^{-1}. 57

4.3 Elastic and final-state j' resolved cross sections as a function of initial rotational level j for a collision energy of 10^{-4} cm^{-1} obtained with the CS approximation for ^{4}He-CO_2. 58

4.4 Elastic cross section and total inelastic cross section as a function of energy for He collisions with CO_2 and various j. 59

4.5 The energy where the elastic cross section is equal to the total inelastic cross section as a function of the rotational level j. 60

4.6 The ratio of the elastic cross section to the total inelastic cross section at different temperatures as a function of j. 61

5.1 Potential energy curves for the interaction of: He(1^1S) with He(3^3S) (top), and He(1^1S) with He(2^3S) and He(2^3P) (bottom). The inset shows the barrier in the $a^3\Sigma_u^+$. 70

5.2 Total elastic cross sections for the collision of: He(1^1S) and He(2^3S) atoms (dotted lines), and He(1^1S) and He(3^3S) atoms (solid lines). 72

5.3 Cross section for excitation transfer from the He(2^3S) atoms to the He(1^1S) gas. 73

5.4 Cross section for the diffusion of He(2^3S) atoms in He(1^1S) gas. 73

List of Tables

2.1 Considered CN molecular states and asymptotic separated-atom and united-atom limit properties. All data in atomic units unless otherwise indicated. . 20

3.1 Rotational Levels of CO_2 44

Chapter 1

Introduction

Collisions between atoms, molecules, electrons, photons, and other particles have important consequences that range from the blue color of the sky to the generation of x-ray emission. They are also very important in the study and understanding of the interactions between these quantum systems. Actually, analyzing the results of crossed beam scattering experiments, is the most practical and dependable method for deducing the interaction potentials between the colliding species. Spectroscopy can also provide parameters from which the potentials can be calculated. However, crossed-beam experiments probe different regions of the interaction potential. Experiments on macroscopic samples do not lead to the potentials acting between the constituents except for rare and simple cases such as for inert gases where the potential can be deduced from thermodynamic data. When the potentials are known, then statistical mechanics can be used to calculate and derive the macroscopic properties of the material.

In crossed-beam experiments, the scattered species are detected at different angles to the incident beam. The density in these collision chambers is very low so single collision events can be assumed. Scattering theory links the observations from these experiments, such as the angular distribution of the particles after the collision, and the interactions responsible for the scattering. Quantum mechanics is the most appropriate framework to describe collisions between quantum systems. Classical mechanics, on the other hand, is still used to provide insights into the problem. Somewhere in between, the semi-classical treatment provides a satisfactory and simplified theory.

Collisions involving exchange in momentum or translational energy only between the colliding species are classified as elastic. Inelastic collisions, on the other hand, result in a change in the internal state of the species involved. That is, an exchange between the translational and rotational, vibrational or electronic energy occurs. A change in electronic state implies an exchange of energy of the order of an electron volt, whereas a change in the vibrational state needs energy of the order of a tenth of an eV. Rotational transitions happen at only 0.01 of an eV. Reactive collisions result in atom rearrangement and/or the production of new species.

1.1 Potential Energy Surfaces and the Born-Oppenheimer Approximation

For a molecule, the Hamiltonian, in the center-of-mass system, can be written as:

$$H = T_n(\vec{Q}) + T_e(\vec{q}) + V(\vec{q}, \vec{Q}), \tag{1.1}$$

where T_n and T_e are the kinetic energy operators for the nuclear and the electronic motions, respectively. That is,

$$T_n = -\sum_k \frac{\hbar^2}{2M_k} \nabla_Q^2, \tag{1.2a}$$

$$T_e = -\sum_i \frac{\hbar^2}{2m} \nabla_q^2, \tag{1.2b}$$

where m is the electronic mass and M_k is the mass of nucleus k. The position vector of the electrons relative to the nuclear center of mass is $\vec{q}$ while $\vec{Q}$ refers to the nuclear coordinates. The electrons are very light compared to the nuclei, hence they can be ignored when calculating the center of mass for the system. As a result, the nuclear center of mass is a good approximation to the total center of mass. The total wave function Ψ depends on the electronic configuration as well as the nuclear coordinates. That is $\Psi = \Psi(\vec{q}, \vec{Q})$. Determining these wave functions and the corresponding energies is not easily achieved by solving the multidimensional Schrödinger equation using the Hamiltonian in 1.1.

In the Born-Oppenheimer approximation, the electronic motion is separated from the nuclear motion based on the assumption that the electrons, because of their much smaller mass, move much faster than the nuclei. If the nuclei were clamped in fixed positions denoted collectively by $\vec{Q}_o$, then the Hamiltonian in 1.1 will consist of the kinetic energy of the electrons and the potential which depends parametrically on $\vec{Q}$. In this case, the Schrödinger equation can be written as:

$$\Big[T_e(\vec{q}) + V(q, Q_o)\Big]\phi_i(\vec{q}, \vec{Q}_o) = E_i'(Q_o)\phi_i(\vec{q}, \vec{Q}_o), \tag{1.3}$$

where $\phi_i(\vec{q}, \vec{Q}_o)$ is the electronic wave function corresponding to energy eigenvalue E_i'. This process can be repeated, and the above equation can be solved for the wave functions and the energies at different nuclear configuration Q_k, and hence with different potential $V(q, Q_k)$. Now, the total wave function can be written as a product of these electronic wave functions and a nuclear wave function χ as:

$$\psi(\vec{q}, \vec{Q}) = \chi(\vec{Q})\phi(\vec{q}, \vec{Q}). \tag{1.4}$$

Substituting ψ given by 1.4 and using the Hamiltonian given by 1.1:

$$\begin{aligned} H\chi(\vec{Q})\phi(\vec{q},\vec{Q}) &= E\chi(\vec{Q})\phi(\vec{q},\vec{Q}) \\ &= \left[T_n(\vec{Q}) + T_e(\vec{q}) + V(q,Q)\right]\chi(\vec{Q})\phi(\vec{q},\vec{Q}) \\ &= \left[-\sum_k \frac{\hbar^2}{2M_k}\nabla_Q^2 + E'(\vec{Q})\right]\chi(\vec{Q})\phi(\vec{q},\vec{Q}). \end{aligned} \tag{1.5}$$

Where the result from 1.3 was used. Now:

$$\nabla_Q^2\chi(\vec{Q})\phi(\vec{q},\vec{Q}) = \phi(\vec{q},\vec{Q})\nabla_Q^2\chi(\vec{Q}) + \chi(\vec{Q})\nabla_Q^2\phi(\vec{q},\vec{Q}) + \nabla_Q\chi(\vec{Q})\cdot\nabla_Q\phi(\vec{q},\vec{Q}). \tag{1.6}$$

In the Born-Oppenheimer approximation, all terms but the first in the equation above are ignored [2]. The justification being, as mentioned before, that the electrons are much lighter than the nuclei. Then, classically, their velocities are large compared to those of the nuclei. As a result, the electronic wave functions change slowly with the nuclear coordinates hence the respective derivatives can be ignored. Consequently, the electronic wave functions can adjust themselves quasi-statistically in response to the nuclear motion. For this reason, these wave functions are called adiabatic. So,

$$\nabla_Q^2\chi(\vec{Q})\phi(\vec{q},\vec{Q}) \sim \phi(\vec{q},\vec{Q})\nabla_Q^2\chi(\vec{Q}). \tag{1.7}$$

Substituting in 1.5 and rearranging yields:

$$\left[-\sum_k \frac{\hbar^2}{2M_k}\nabla_Q^2 + E'(\vec{Q})\right]\chi(\vec{Q}) = E\chi(\vec{Q}). \tag{1.8}$$

This is the Schrödinger equation for the nuclear wave functions. It shows that the nuclei move in an effective potential, E', which is the energy eigenvalue, as a function of nuclear coordinates, of a particular electronic configuration.

1.2 Adiabatic vs. Diabatic Representation and the Multichannel Equations

In scattering problems, $3N$-3 coordinates are needed to describe the state of the system where N is the number of colliding objects, whether they are molecules, atoms, electrons, ... or any combination. In the center-of-mass frame, the collision between two or more objects is equivalent to the scattering of an object with mass μ from the interaction potential where μ is the reduced mass of the system. It is customary and mathematically convenient to separate the relative position, i. e. the position relative to the center-of-mass, vector, $\vec{r}$, from the internal coordinates, referred to collectively here as $\vec{\rho}$. The Hamiltonian can then be written as [3]:

$$H = H_{int}(\vec{\rho}) - \frac{\hbar^2}{2\mu}\nabla_r^2 + V(\vec{r}, \vec{\rho}), \tag{1.9}$$

where $V(\vec{r}, \vec{\rho})$ is the interaction potential which vanishes, by definition, when the objects under consideration are at infinite distance from each other. That is:

$$\lim_{r\to\infty} V(\vec{r}, \vec{\rho}) = 0. \tag{1.10}$$

The time independent Schrödinger equation:

$$H\Psi(\vec{r}, \vec{\rho}) = E\Psi(\vec{r}, \vec{\rho}), \tag{1.11}$$

where E is the total energy of the system in the center-of-mass coordinates, can then be solved utilizing different approximations. The two most important and frequently used will be discussed here.

The total wave function Ψ can be expanded in terms of the eigenstates of H_{int}, that is:

$$\Psi(\vec{r}, \vec{\rho}) = \sum_j \psi_j(\vec{r})\phi_j(\vec{\rho}), \tag{1.12}$$

where

$$H_{int}(\vec{\rho})\phi_j(\vec{\rho}) = E_j\phi_j(\vec{\rho}). \tag{1.13}$$

Substituting in 1.9 and utilizing the orthonormality of $\phi_j(\vec{\rho})$ yields

$$\Big[\nabla_r^2 + k_i^2\Big]\psi_i(\vec{r}) = \sum_j V_{ij}(\vec{r})\psi_j(\vec{r}), \tag{1.14}$$

where

$$\begin{aligned} k_i^2 &= 2\mu(E - E_i)/\hbar^2; \\ V_{ij}(\vec{r}) &= (2\mu/\hbar^2)\int \phi_i^*(\vec{\rho})V(\vec{r}, \vec{\rho})\phi_j(\vec{\rho})\, d\vec{\rho}. \end{aligned} \tag{1.15}$$

Alternatively, the total wave function can be expanded in terms of the eigenfunctions of the full internal Hamiltonian at a given relative position, $\vec{r}$. In this case:

$$\Psi(\vec{r}, \vec{\rho}) = \sum_j \tilde{\psi}_j(\vec{r})\tilde{\phi}_j(\vec{r}, \vec{\rho}), \tag{1.16}$$

where

$$\Big[H_{int}(\vec{\rho}) + V(\vec{r}, \vec{\rho})\Big]\tilde{\phi}_j(\vec{r}, \vec{\rho}) = \tilde{E}_j(r)\tilde{\phi}_j(\vec{r}, \vec{\rho}). \tag{1.17}$$

$\tilde{\phi}_j$ and $\tilde{E}_j$ depend parametrically on $\vec{r}$. Since the potential vanishes at infinite separation, then, as r $\rightarrow \infty$

$$\tilde{\phi}_j(\vec{r}, \vec{\rho}) \sim \phi_j(\vec{\rho}) \tag{1.18a}$$

$$\tilde{E}_j(r) \sim E_j. \tag{1.18b}$$

Using this expansion and utilizing the orthonormality of the eigenfunctions yields the equivalent for 1.14:

$$\left[\nabla_r^2 + k_i^2\right]\tilde{\psi}_i(\vec{r}) = \sum_j \left[R_{ij}(\vec{r}) \cdot \nabla_r + P_{ij}(\vec{r})\right]\tilde{\psi}_j(\vec{r}), \tag{1.19}$$

where

$$\begin{aligned} k_i^2(\vec{r}) &= 2\mu(E - \tilde{E}_i(\vec{r}))/\hbar^2; \\ R_{ij}(\vec{r}) &= -2\int \tilde{\phi}_i^*(\vec{r}, \vec{\rho})\nabla_r\tilde{\phi}_j(\vec{r}, \vec{\rho})\, d\rho = -2\langle\tilde{\phi}_i \mid \nabla_r \mid \tilde{\phi}_j\rangle, \\ P_{ij}(\vec{r}) &= -\int \tilde{\phi}_i^*(\vec{r}, \vec{\rho})\nabla_r^2\tilde{\phi}_j(\vec{r}, \vec{\rho})\, d\rho = -\langle\tilde{\phi}_i \mid \nabla_r^2 \mid \tilde{\phi}_j\rangle. \end{aligned} \tag{1.20}$$

The basis $\tilde{\phi}_j(\vec{r}, \vec{\rho})$ depend parametrically on the relative position $\vec{r}$. They resemble the adiabatic functions used in the Born-Oppenheimer approximation. Hence they are known as the adiabatic basis. By comparison, the $\phi_j(\vec{\rho})$ are known as the diabatic basis. Each of equations 1.14 and 1.19, is a set of equations, one for each basis function or a channel. Hence the name multichannel equations. In the diabatic representation, the channels are coupled together by the off-diagonal elements of the interaction potential, whereas the coupling is through the kinetic energy for the relative motion in the adiabatic representation. k_i as defined in 1.15 and 1.20 is the channel wave number. When $E > E_i$, the i^{th} channel is said to be open, because the molecule can emerge in that state after the interaction. Otherwise, the channel is closed when the wave number is imaginary.

The diabatic and adiabatic bases form complete sets, so either one provides an exact representation of the wave function. However, in practice, a finite basis is used in the expansions 1.12 and 1.16. The result is a finite number of multichannel equations called the close-coupling equations. The choice of basis set depends on the problem to be solved. For example, when the internal motion of the colliding partners can be assumed fast compared to the relative motion, then the adiabatic representation is more appropriate to use. The accuracy and the computation resources determine the number of basis functions to include. In general, the adiabatic basis functions vary slowly with r hence, the kinetic energy coupling terms in 1.19 are small. Therefore fewer terms are needed in the adiabatic representation 1.16 to achieve convergence. However, equation 1.17 must be solved for the relevant range of r to obtain the adiabatic basis. This is not an easy task. As a result, most calculations use the diabatic basis.

1.3 Scattering: a General Review

In general terms, the wave function of the system outside the scattering region, that is where the interaction potential is effectively zero, can be written as a combination of the incident wave function and the scattered wave function as follows:

$$\Psi(r,\rho)_{r\to\infty} \sim \phi_j(\rho)e^{ik_j z} + \frac{1}{r}\sum_{j'} f_{jj'}(\Omega)\phi_{j'}(\rho)e^{ik_{j'}r}, \tag{1.21}$$

where ρ stands collectively for all internal coordinates needed to describe the internal state designated by ϕ. $f_{jj'}$ is the scattering amplitude which depends on the scattering solid angle Ω. If the scattering has cylindrical symmetry about the z-axis, as in the case of a central force, the scattering amplitude is a function of the polar angle, θ, only. The cross section for a system initially in state j to be scattered to state j' is the ratio of the scattered flux to that of the incident flux which translates to:

$$\sigma_{jj'}(\Omega) = \left(\frac{k_{j'}}{k_j}\right)|f_{jj'}|^2 \tag{1.22}$$

An alternative, but related, description involves the scattering matrix ***S***. The state of the system before the collision, $z \to -\infty$, can be written in terms of the eigenfunctions $\phi(\rho)$ as:

$$\Phi(\rho) = \sum_j c_j \phi_j(\rho), \tag{1.23}$$

and after the collision, $z \to \infty$, it becomes

$$\Phi^{'}(\rho) = \sum_j c_j' \phi_j(\rho). \tag{1.24}$$

The ***S*** matrix is defined by

$$\mathbf{C}' = \mathbf{SC}, \tag{1.25}$$

where ***C*** and ***C'*** are the column vectors of the coefficients before and after the collision respectively. The ***S*** matrix is a function of the total energy and it depends on the system's total angular momentum J.

The probability is conserved, that is:

$$\sum_j |c_j|^2 = 1 = \sum_j |c_j'|^2. \tag{1.26}$$

Then

$$
\begin{aligned}
\mathbf{C'^{\dagger}C'} &= (\mathbf{SC})^{\dagger}\mathbf{SC} && = 1, \\
\mathbf{C'^{\dagger}C'} &= \mathbf{C^{\dagger}S^{\dagger}SC} && = 1, \\
\implies \quad & \mathbf{S^{\dagger}S = I} \quad \textbf{or} \quad \mathbf{S^{\dagger} = S^{-1}} &&
\end{aligned}
\tag{1.27}
$$

where the (†) stands for the adjoint, transpose and complex conjugate, or hermitian conjugate. **S** is then a unitary matrix. $|S_{jj'}|^2$ is the probability of transition between states j, and j'. Time reversal shows that $|S_{jj'}|^2$ is equal to $|S_{j'j}|^2$. Hence, **S** is also a symmetric matrix.

Generally, the wave functions above are determined from solving coupled Schrödinger equations. From these wave functions, the scattering matrix elements are determined which are then used to calculate the cross section. For a given J,

$$\sigma^J_{jj'}(E_j) = \frac{\pi}{k^2}\left|\delta_{jj'} - S^J_{jj'}\right|^2. \tag{1.28}$$

Then

$$\sigma_{jj'}(E_j) = \sum_{J=J_{min}}^{J=J_{max}} \sigma^J_{jj'}(E_j). \tag{1.29}$$

The rate coefficient for that transition can then be obtained by averaging over the range of velocities available. Often a Maxwell-Boltzmann distribution is adopted so the rate coefficient is given by:

$$r_{j\to j'}(T) = \left(\frac{8k_BT}{\pi\mu}\right)^{1/2} \frac{1}{(k_BT)^2} \int_0^\infty \sigma_{jj'}(E_j) e^{\left(-\frac{E_j}{k_BT}\right)} E_j \, dE_j, \tag{1.30}$$

where k_B is the Boltzmann constant and T is the kinetic temperature of the gas. The total quenching rate coefficient is calculated by adding up contributions from all possible exit channels, so that:

$$r_j = \sum_{j'} r_{j\to j'}(T). \tag{1.31}$$

Behavior at Low Temperature and the Wigner Laws

If the interaction potential goes to zero as $1/r^{2+\epsilon}$ and $\epsilon > 0$, then the energy dependence of the cross section follows simple rules derived by Wigner [4]:

$$\sigma_{nl\to nl'} \sim v_n^{2(l+l')}, \tag{1.32a}$$

$$\sigma_{nl\to n'l'} \sim v_n^{2l-1}, \tag{1.32b}$$

where v_n is the relative velocity, l is the angular momentum of the collision, and n is a collective index that describes the state. In our case, n is just the rotational quantum number j. At cold temperatures or low collision energies, the scattering is dominated by the s-wave, that is the $l = 0$ term. It follows then from the equations above that for elastic scattering, i.e. $n = n'$ and $l = l'$, the cross section approaches a constant. However, for the inelastic case, the cross section varies as the inverse velocity. This is known as Wigner threshold behavior.

1.4 Photodissociation

Photodissociation is, as the name suggests, the fragmentation of molecules upon the absorption of photons. It is the first step in many chain reactions such as the ozone-oxygen cycle in the atmosphere. Many chemical lasers achieve population inversion by photodissociation [5]. The iodine laser discovered by Kasper and Pimentel [6] is an example. Iodine is produced by the photodissociation of CH_3I. However, the populations of the two electronic states, ${}^2P_{1/2}$ and ${}^2P_{3/2}$, of the produced iodine are usually inverted. The laser subsequently operates on the $^2P_{1/2} \rightarrow\ ^2P_{3/2}$ electronic transition. Photodissociation is the main process of destruction of molecules in regions such as diffuse and translucent interstellar clouds where intense ultraviolet radiation exists [7]. In addition to the applications mentioned and on a more fundamental level, photodissociation can be used to investigate molecular dynamics such as the breaking and construction of bonds, internal energy transfer between the different modes in a molecule, and radiationless transitions with precision. Bond breaking can be studied experimentally using single quantum states. In such experiments, usually three lasers are used [5]. One laser is used to prepare the molecule in the specific ro-vibrational state in the ground electronic state. Absorbing radiation from another laser excites the molecule into the continuum. A third laser is used to probe the products. Photodissociation energy can be as small as several thousandths of an eV for van der Waals molecules bound by the weak long-range forces. For chemically bound molecules, the photodissociation energy is typically $1 - 10$ eV.

Absorbing a photon causes a molecule to jump to an excited state constrained by angular momentum selection rules and the wavelength of the photon. When in the excited state, the molecule can follow different paths to dissociation. The rate of dissociation depends on the cross sections for all these possibilities and on the intensity and shape of the radiation field.

Let AB be the parent molecule, then the photodissociation process can be written as [5]:

$$AB + N_{photon}\hbar\omega \rightarrow (AB)^* \rightarrow A(\alpha) + B(\beta), \tag{1.33}$$

where N is the number of photons absorbed, $(AB)^*$ is the excited complex, α and β represent the internal state of the fragments A and B respectively. The photodissociation is described as direct when the molecule dissociates immediately after excitation. That is the life time of the excited complex is very short compared to the vibrational period in that bond. This happens when the energy surface of the excited state is repulsive along the coordinate associated with the bond. In this case, there are no potential barriers that prevent the molecule from moving down the potential slope so to speak. If such a barrier exists, then the molecule spends longer time in the excited state. It may subsequently dissociate indirectly by electronic predissociation, vibrational predissociation or unimolecular reactions [5]. Direct photodissociation can be treated by classical mechanics. However, a full quantum-mechanical description is needed for the other types.

Photodissociation vs. Scattering

Following the notation in equation 1.33, if A and B were two entities prepared at a given internal state at infinity, then upon collision or scattering, they form an excited complex $(AB)^*$ which decays subsequently through the available channels, $A(\alpha)$ and $B(\beta)$ in this case. The second half of the dissociation process as in equation 1.33 is the same as the second part of the full collision as described. Hence, photodissociation is sometimes called a half-collision.

Total angular momentum, orbital plus rotational, is conserved during a collision or photodissociation event. Calculating the cross section, in both cases, usually involves averaging over total angular momentum states denoted by the quantum number J. Each state weighted by $(2J+1)$. In collisions, a large number of J, called partial wave, is needed. In photodissociation, the available total angular momentum states are constrained by the dipole selection rule:

$$\Delta J = J_i - J_f = 0 \quad or \quad \pm 1. \tag{1.34}$$

This reduces the number of total angular momentum states needed to be taken into account in the case for photodissociation. This consequently reduces the numerical effort.

The total energy in photodissociation can be controlled by varying the wavelength of the radiation used. This enables the detection of resonances and other structures in the spectrum. However, in case of collision between atoms or molecules, the total energy is not easily controlled experimentally.

1.5 Molecules in the Interstellar Medium

Spectral analysis is an important tool in the study of the chemical and physical state of interstellar clouds. Identifying the species is one piece of information extracted from such spectra. On the other hand, knowledge of the abundances of these species, which are proportional to the strengths of the spectral lines, are very important in understanding the environment of interstellar clouds [8]. Abundances depend, among other factors, on the production and destruction processes. Photodissociation is usually the dominant destruction mechanism for most neutral molecules in diffuse and translucent clouds, photodissociation regions (PDRs), x-ray dominated regions (XDRs), the surfaces of protoplanetary disks (PPDs), circumstellar shells, and other UV-irradiated environments see, for example [9, 10]. In Chapter 2, the photodissociation of CN is considered.

The dust particles in the dense clouds scatter and absorb most of the star light and render the clouds invisible to the eye. As a result, molecular species are identified almost exclusively from their rotational spectra. These transitions correspond to wavelengths of the order of a millimeter which suffer negligible scattering or absorption by the grains. Also, millimeter radiation is not attenuated by the Earth's atmosphere. Moreover, the resolution of lines is much better than for higher energy transitions. The gas density and temperature can be derived from the relative intensities of the rotational emission lines. When the density is low and collisions are rare, the populations of the rotational levels result from equilibrium with the pervasive radiation field. However, when the density is high, collisions determine the populations of the rotational levels. In this case, the temperature deduced from the relative populations corresponds to the kinetic (or translational) temperature of the gas [11, 12]. An interesting case is that of the cyanogen molecule (CN). CN was among the first molecules detected in the ISM by McKellar[13]. He estimated the excitation temperature of CN to be 2.3 K. However, it was not explained [14] until the discovery of the cosmic microwave background by Dicke et al. [15] and Penzias and Wilson [16, 17, 18] in 1965. Now, it is accepted that the relative populations of the rotational levels of CN are the result of radiative equilibrium with the CMB. Considering that the existence of CMB is an important prediction of the Big Bang theory, the rotational spectra of molecules in space is a valuable source of information.

The density divide between the radiative equilibrium regime and the collisional one is not simple or unique for all molecules or even for all transitions of the same molecule. However, it is possible to deduce a critical gas density at which the Einstein coefficient for spontaneous emission is equal to the frequency of collisions that transfer the molecule to different rotational levels. The frequency of collision is calculated from the rate coefficient for that transition and the density of the gas. In Chapter 3, the rotational relaxation of CO_2 resulting from collisions with He atoms is discussed and the rate coefficients are calculated.

A delicate balance between processes that destroy the molecules and those producing them dictates the molecular abundances in different astronomical environments in which these molecules exist. Many models to predict or produce the observed abundances of the molecules exist. They consist of a large number of rate equations which are differential equations that describe the change in concentration of any given species as a result of the destructive and synthesizing processes. The rate coefficients, derived from the cross sections are needed inputs to such models.

Chapter 2

Photodissociation of Cyanogen[1]

In a study of translucent clouds, [19] found that the observed abundances of CN and C_2 could not be reproduced by their models without significantly adjusting the photodissociation rates. In the former case, the photodissociation calculations of [1], obtained from the ground rovibrational level of the electronic X $^2\Sigma^+$ state, were adopted. Here we revisit the photodissociation of CN by performing calculations over a large photon energy range and from all ro-vibrational levels $v''N''$,

$$\mathrm{CN}(X\ ^2\Sigma^+, v'', N'') \quad + \quad h\nu \quad \rightarrow \quad \mathrm{C} \quad + \quad \mathrm{N}. \tag{2.1}$$

Ab initio potentials and transition moment functions were adopted from [1], but adjusted and extended as appropriate to known experimental and theoretical constraints. Cross sections were computed for the $^2\Sigma^+(4) \leftarrow$ X $^2\Sigma^+$, $^2\Sigma^+(5) \leftarrow$ X $^2\Sigma^+$, $^2\Pi(4) \leftarrow$ X $^2\Sigma^+$, and $^2\Pi(5) \leftarrow$ X $^2\Sigma^+$ electronic transitions. Atomic units are used throughout unless otherwise stated.

---

[1] Based on W. H. al-Qady & P. C. Stancil. Submitted to the Astrophys. J. (under review)

2.1 Photodissociation Cross Sections

The partial photodissociation cross section for a transition from rovibrational state $v''N''$ of electronic state i to the continuum of electronic state f can be written as [7, 20]

$$\sigma_{v''N''} = 2.689 \times 10^{-18}\ \Delta E_{k'N',v''N''} \frac{g}{2N''+1} \sum_{N'=N''-1}^{N''+1} S_{N'} |D^{fi}_{k'N',v''N''}|^2 \text{ cm}^2, \tag{2.2}$$

where $\Delta E_{k'N',v''N''}$ is the energy of the photon absorbed in the transition, $D^{fi}_{k'N',v''N''}$ is the matrix element $\langle \chi_{k'N'}(R)|D^{fi}(R)|\chi_{v''N''}(R)\rangle$, of the electric dipole transition moment responsible for absorption from the initial state i with wave function $\chi_{v''N''}(R)$ into the f electronic state, v is the vibrational quantum number, N is the angular momentum for nuclear motion, and g is the molecular state degeneracy factor given by

$$g = \frac{2-\delta_{0,\Lambda'+\Lambda''}}{2-\delta_{0,\Lambda''}}. \tag{2.3}$$

Here, we neglect spin-splitting in the electronic ground state and Λ-doubling in excited Π states. The latter is accounted for through the factor g assuming the final Π continuum states are degenerate.

The continuum wave functions $\chi_{k'N'}(R)$ are normalized such that they behave asymptotically as

$$\chi_{k'N'}(R) \sim \sin(k'R - \frac{\pi}{2}N' + \delta_{N'}), \tag{2.4}$$

where $\delta_{N'}$ is the phase shift. The $S_{N'}$'s in equation (2.2) are the Hönl-London factors defined, for a $\Sigma \leftarrow \Sigma$ transition as

$$S_{N'}(N'') \quad = \quad \begin{cases} N'', & N' = N''-1 \text{ (P branch)} \\ N''+1, & N' = N''+1 \text{ (R branch)}, \end{cases} \tag{2.5}$$

and for a $\Pi \leftarrow \Sigma$ transition as

$$S_{N'}(N'') = \begin{cases} (N''-1)/2, & N' = N''-1 \text{ (P branch)} \\ (2N''+1)/2, & N' = N'' \quad \text{ (Q branch)} \\ (N''+2)/2, & N' = N''+1 \text{ (R branch)}, \end{cases} \tag{2.6}$$

according to the convention of [21].

Continuum wave functions $\chi_{k'N'}$ for the $^2\Sigma^+(4)$, $^2\Sigma^+(5)$, $^2\Pi(4)$, and $^2\Pi(5)$ states and bound wave functions $\chi_{v''N''}$ for the X $^2\Sigma^+$ state were obtained by solving the radial Schrödinger equation using the Numerov method [22]. Wave functions were obtained on a grid with a stepsize of 3×10^{-4} a$_o$ over the internuclear distance range $0.5 \leq R \leq 200$ a$_o$.

2.2 Potential Energy and Dipole Transition Moment Functions

Ab initio potential energies and dipole transition moments from [1] were used to calculate the partial cross sections for CN presented in this work. They reported potential energies for internuclear distances $R = 1.90$ a$_o$ to $R = 3.70$ a$_o$. For $R > 3.7$ a$_o$, the potentials were extrapolated by fitting to the long-range interaction potential

$$V(R) = -\frac{C_5}{R^5} - \frac{C_6}{R^6 - Q^2R^4} \tag{2.7}$$

[23]. The adopted values of the coefficients C_5 and C_6 are shown in Table 2.1. As we are unaware of any previous van der Waals coefficient calculations for CN, we approximated them following the procedures of [24] and [25]. C_6 was estimated for X $^2\Sigma^+$ using the London formula and known ground state dipole polarizabilities of C and N. Estimates were made of the excited state C and N polarizabilities considering only bound-bound atomic transitions

and used to approximate C_6 for the CN excited states. As the resulting C_6 estimates are of similar magnitude, the X $^2\Sigma^+$ C_6 was used for all molecular states. $Q = 2.34$ was estimated for the ground state and the same value used for other states. The sign of the C_5 coefficient was then obtained following [25] with the magnitude computed by fitting the longest-range potential data of [1], but keeping C_6 and Q fixed. The estimated values of C_6 can be compared to 29.651 and 24.80 obtained for the X $^1\Sigma^+$ and A $^1\Pi$ states of CO, respectively [26]. Further, C_6 for the four lowest electronics states of C_2, X $^1\Sigma_g^+$ (62.98), a $^3\Pi_u$ (61.54), b $^3\Sigma_g^-$ (60.28), and A $^1\Pi_u$ (61.54), are all very similar [27]. While for the C_2 a $^3\Pi_u$, [27] estimated $C_5 = 13.5$.

For $R < 3.70$ a$_o$, the potential curves were fitted to the short-range interaction exponential form $A\exp(-BR) + C$. The complete X $^2\Sigma^+$ potential was further forced to give exact agreement with the experimental dissociation energy of 7.76 eV [28] by adjusting the matching of the ab initio data to the long-range form relation (2.7). While no experimental information is available for the excited states $^2\Sigma^+(4)$, $^2\Sigma^+(5)$, $^2\Pi(4)$, and $^2\Pi(5)$, their potentials were shifted to match experimental asymptotic atomic energies [29] as given in Table 2.1 and shown in Figure 2.1. While this procedure results in some uncertainty, it ensures that the photodissociation cross section thresholds from X $^2\Sigma^+$ $(v'' = 0, N'' = 0)$ agree exactly with available experimental data.

In a like manner, the transition dipole moment functions were extended beyond the ab initio data given in [1] by fitting at long-range to the form $A\exp(-BR)$. At short-range the fit was made to a quadratic which terminated at $R = 0$ to the transition dipole moments for Al as given in Table 2.1.

Table 2.1: Considered CN molecular states and asymptotic separated-atom and united-atom limit properties. All data in atomic units unless otherwise indicated.

Molec.	Separated-atom				United-atom Al	
State	Atomic states	Energy (eV)[a]	C_5[b]	C_6[c]	State	Dipole mom.[d]
$X\ ^2\Sigma^+$	C($2s^22p^2\ ^3P$) + N($2s^22p^3\ ^4S^0$)	0.00	0	30.84	$3s^23p\ ^2P^0$	-
$^2\Pi(4)$	C($2s^22p^2\ ^3P$) + N($2s^22p^3\ ^2P^0$)	3.571935	-5	30.84	$3s^2(^1S)nd\ ^2D$	1.6
$^2\Sigma^+(4)$	C($2s^22p^2\ ^1D$) + N($2s^22p^3\ ^2D^0$)	3.644021	50	30.84	$3s^24p\ ^2P^0$	0
$^2\Pi(5)$	C($2s^22p^2\ ^1D$) + N($2s^22p^3\ ^2D^0$)	3.644021	14	30.84	$3s^25p\ ^2P^0$	0
$^2\Sigma^+(5)$	C($2s^22p^2\ ^1D$) + N($2s^22p^3\ ^2P^0$)	4.835661	26	30.84	$3s^25s\ ^2S$	0.858

---

[a] Experimental data from [29].
[b] Estimated. See text for details.
[c] Estimated. See text for details.
[d] Experimental data from [29].

2.3 Results and Discussion

A sample of results for the partial cross sections $\sigma_{v''N''}$ for transitions from different rovibrational levels of the X $^2\Sigma^+$ electronic state are shown in Figures 2.2-2.5 [2]. Only the final electronic states $^2\Sigma^+(4)$, $^2\Sigma^+(5)$, $^2\Pi(4)$, and $^2\Pi(5)$ were considered as transitions to low-lying states are either dominated by bound-bound transitions or were found by [1] to give negligible photodissociation cross sections. Figure 2.2 shows the results obtained for transitions from the lowest rovibrational level $v'' = 0$, $N'' = 0$ of the ground electronic state X $^2\Sigma^+$ compared to the cross sections of [1], where the latter is a sum over all final states.

In agreement with [1], we find that the cross section at the longest wavelengths is dominated by transition to the $^2\Pi(5)$. However, correctly accounting for the separated-atom energies, we obtain the threshold for this transition at 1087 Å (11.4 eV) compared to $\sim$ 1040 Å (12 eV) used by [1]. We also find a second strong resonance near 1030 Å due to a quasi-bound state in the upper potential energy curve. The $^2\Pi(4)$ has a longer wavelength threshold (1094 Å or 11.3 eV), but its cross section near threshold is more than an order of magnitude

---

[2] Complete data for all computed photodissociation cross sections are available online at the UGA Molecular Opacity Project database website, `http://www.physast.uga.edu/ugamop/`

smaller as seen in the inset to Figure 2.2. For the $^2\Sigma^+(5)$ cross section, our results appear to be smaller than predicted by [1] and shifted to shorter wavelengths, though it is not clear from their summed cross section the contribution of individual components. The $^2\Sigma^+(4)$ cross section is smaller than the cross section for the other transitions (except the $^2\Pi(4)$), but it reaches a peak magnitude near 960 Å .

Overall the current CN cross section from the ground rovibrational level is about a factor of two smaller than that obtained by [1], which may help to reduce the discrepancy for the CN abundance in translucent molecular cloud models [19]. Further, the present cross sections are highly oscillatory. This is to be expected as the reduced mass of CN is large and the final continuum wave functions fluctuate rapidly as the repulsive walls of the potentials are ascended.

Figures 2.3 and 2.4 show the partial cross sections for transitions from the vibrational levels $v'' = 0$ and $v'' = 20$ with different N'' for $^2\Sigma^+(5)$ and $^2\Pi(5)$, respectively. As N'' and/or v'' increases, the threshold wavelength increases as expected. For $v'' = 0$, cross sections generally become less oscillatory with increasing N'', while for $v'' = 20$, the oscillations and resonances are seen to persist. Partial cross sections for the transitions $^2\Sigma^+(5) \leftarrow \text{X}\ ^2\Sigma^+$ and $^2\Pi(5) \leftarrow \text{X}\ ^2\Sigma^+$ for various v'' with $N'' = 0$ are shown in Figure 2.5. As expected the threshold shifts to longer wavelength as v'' increases, but with the overall magnitude decreasing. Similar trends are found for the other electronic transitions.

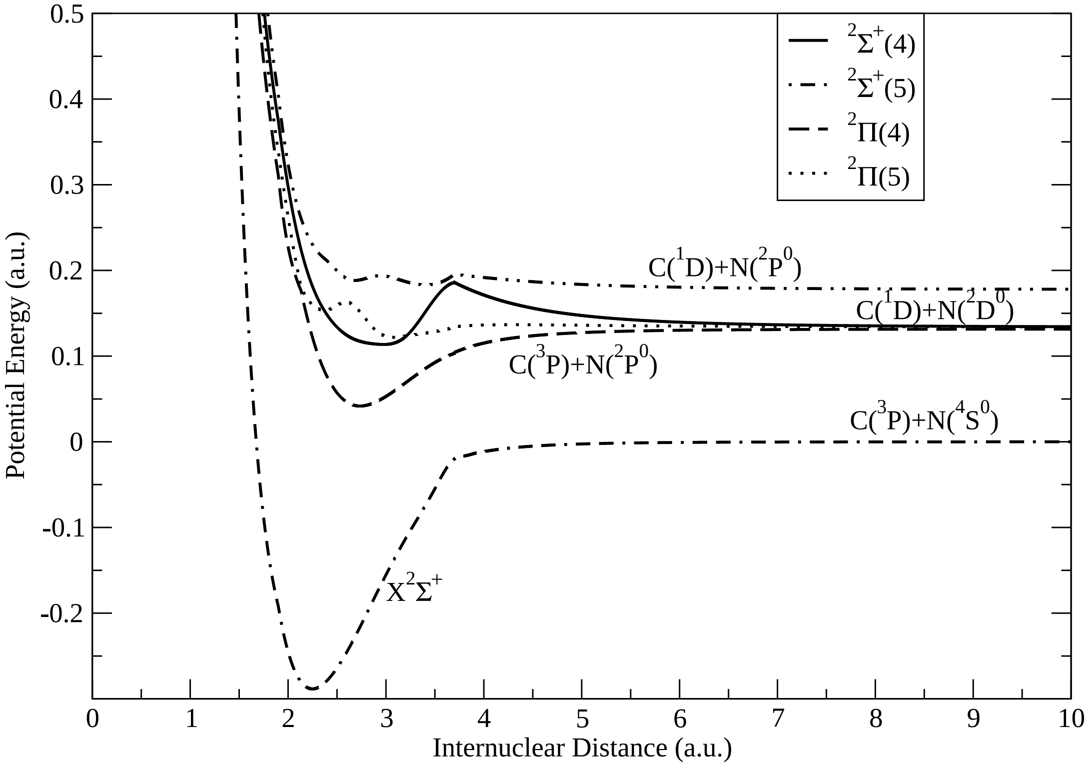

Figure 2.1: Potential energy curves for the low-lying doublet electronic states of CN considered in this work which are dipole-connected to the X $^2\Sigma^+$ ground state. The notation follows that of [1].

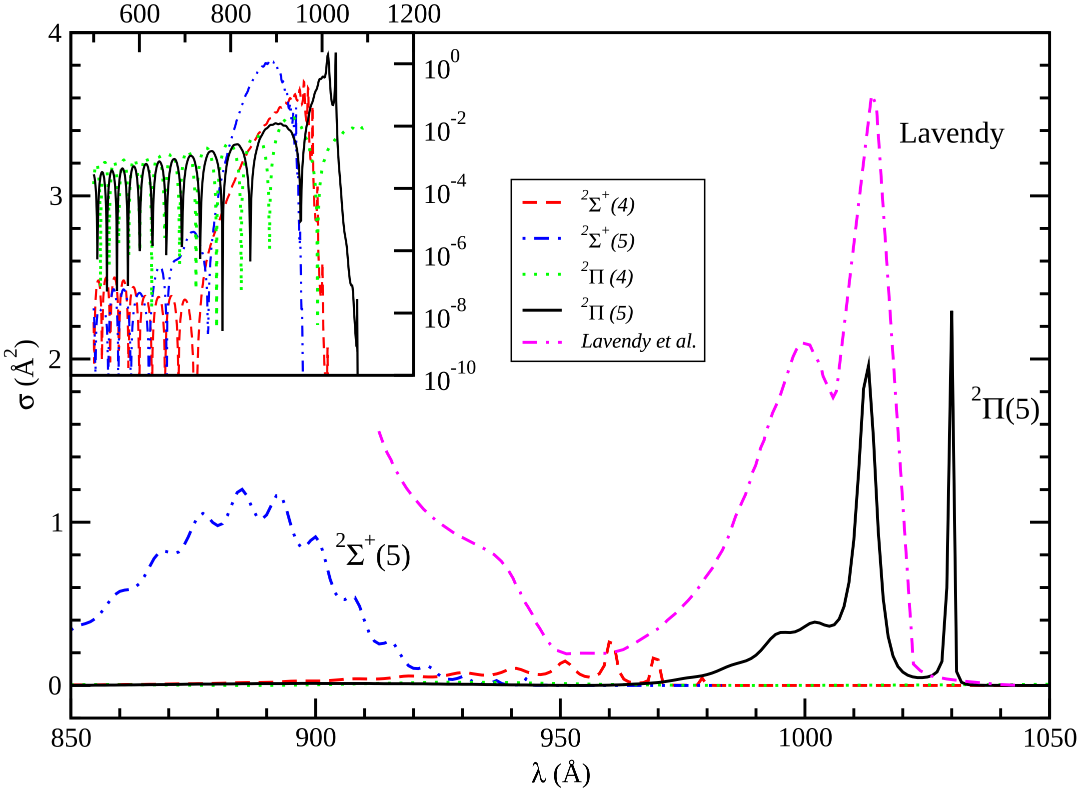

Figure 2.2: CN photodissociation partial cross sections as a function of wavelength for the transitions $^2\Sigma^+(4) \leftarrow \mathrm{X}\ ^2\Sigma^+$, $^2\Sigma^+(5) \leftarrow \mathrm{X}\ ^2\Sigma^+$, $^2\Pi(4) \leftarrow \mathrm{X}\ ^2\Sigma^+$, and $^2\Pi(5) \leftarrow \mathrm{X}\ ^2\Sigma^+$ from the ground rovibrational level $(v'' = 0, N'' = 0)$ of the ground electronic state compared to the summed cross section of [1]. Inset is the same on a log-linear scale.

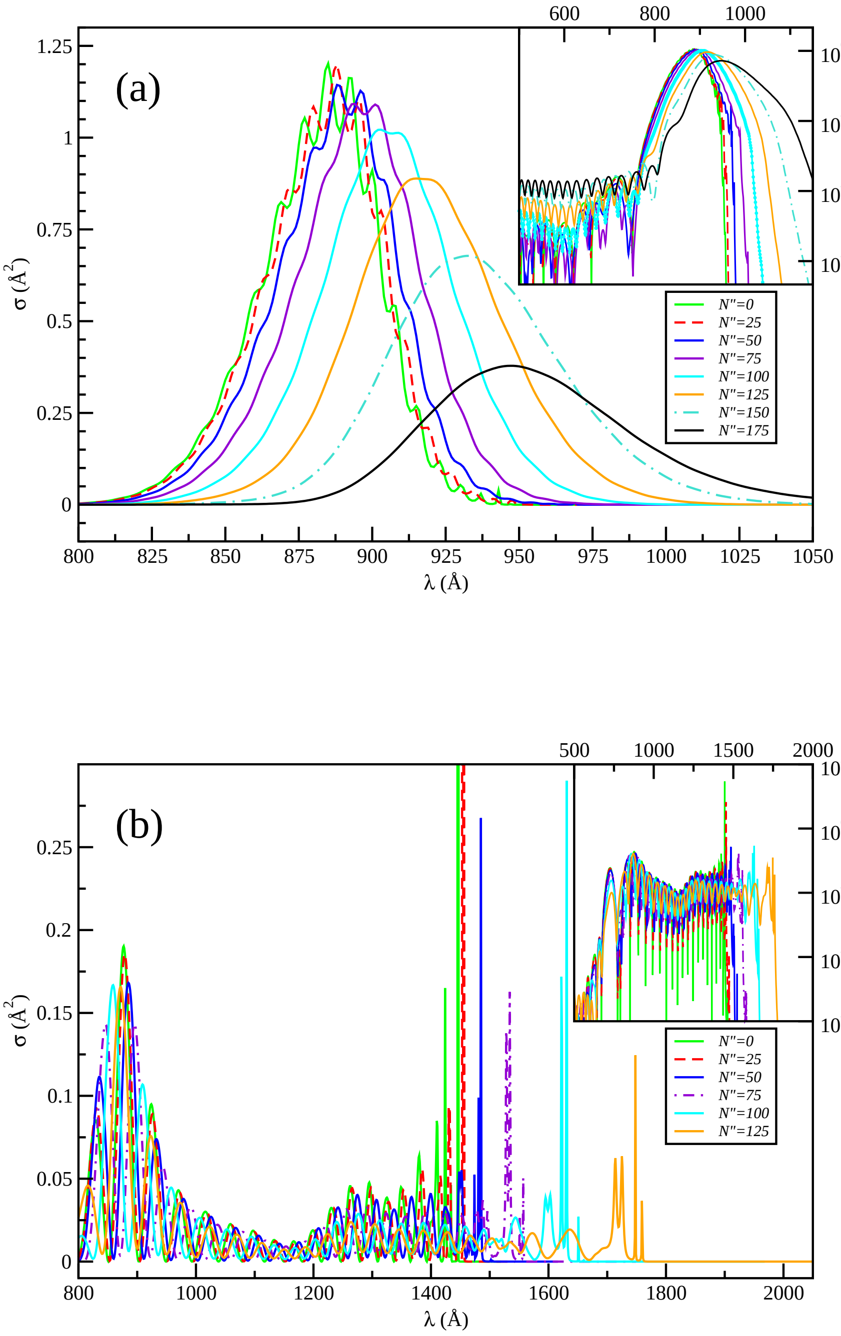

Figure 2.3: CN photodissociation partial cross sections as a function of wavelength for the transition $^2\Sigma^+(5) \leftarrow \mathrm{X}\ ^2\Sigma^+$ from two vibrational levels with different rotational quantum number N'' of the ground electronic state. (a) $v'' = 0$. (b) $v'' = 20$.

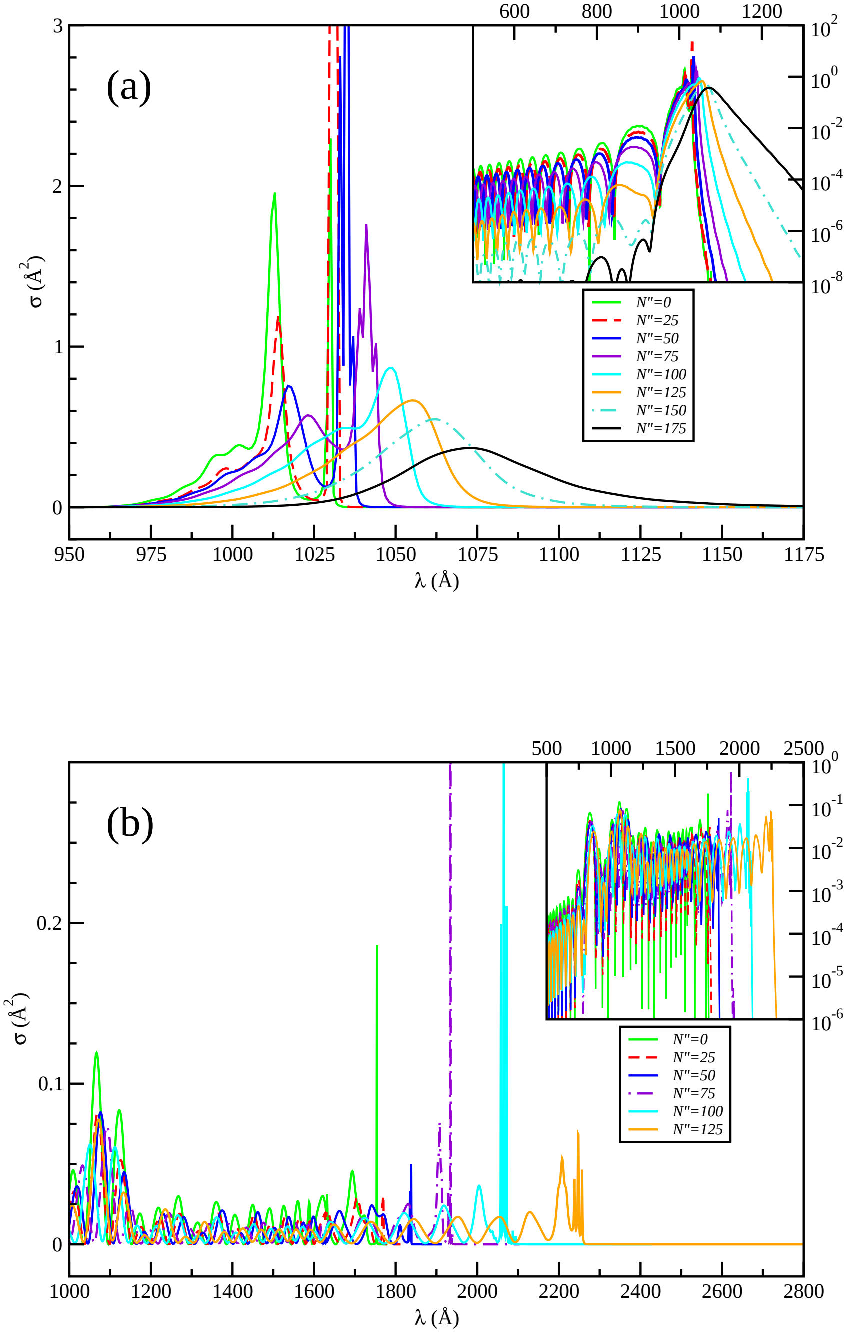

Figure 2.4: CN photodissociation partial cross sections as a function of wavelength for the transition $^2\Pi(5) \leftarrow$ X $^2\Sigma^+$ from two vibrational levels with different rotational quantum number N'' of the ground electronic state. (a) $v'' = 0$. (b) $v'' = 20$

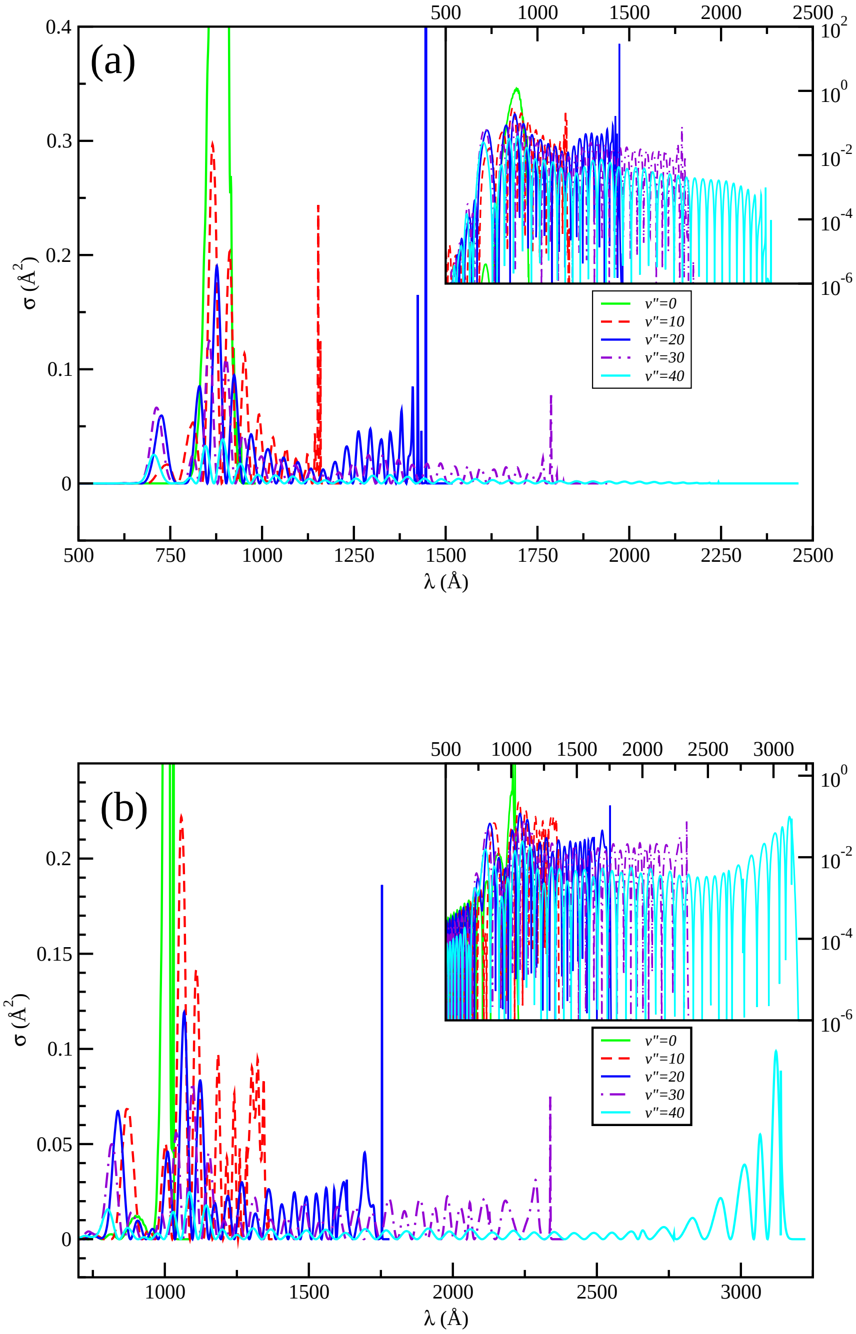

Figure 2.5: CN photodissociation partial cross sections as a function of wavelength for the transition from different vibrational levels v'' with the rotational quantum number $N'' = 0$ of the ground electronic state. (a) $^2\Sigma^+(5) \leftarrow \mathrm{X}\ ^2\Sigma^+$. (b) $^2\Pi(5) \leftarrow \mathrm{X}\ ^2\Sigma^+$.

2.4 Astrophysical Applications

In nearly all environments, except dense regions, the abundances of atoms and molecules are limited by efficient photo-destruction reactions due to the local radiation field. However, photo-destruction rates are dependent not only on the properties of the affected species (via the cross section), but also on local conditions including the intensity and wavelength dependence of the radiation field. The radiation field is attenuated with depth into a cloud due to wavelength-dependent absorption by the dominant atoms (H), molecules (H_2 and possibly CO), and grains. While this is a very complicated problem, the issue has been addressed, in large part, in a pragmatic fashion in most astrochemical models. The majority of astrochemical models include photo-destruction through pre-computed exponentially-attenuated fitted photo-rates which can, for example, be found in such databases as UMIST [30]. The photo-rates are given as a function of visual extinction A_{v} and have primarily been taken from the calculations/compilations of [31] and [32]. These calculations were performed for plane-parallel clouds illuminated by an average interstellar radiation field including UV radiation attenuation due to scattering and absorption by dust grains. The grain model assumed the average interstellar graphite-silicate grain mixture of [33] with the grain optical properties taken from [34]. The adoption of these pre-computed photorates have allowed for significant advancement in modeling by considerably reducing the problem to the solution of coupled rate equations. However, quoting [32] “Our results apply strictly to the ‘average cloud’ in a region of the diffuse interstellar medium where R_V=3.1.” This is in contrast, for example, to the average value of $R_V = 4.05$ with a scatter of ± 0.8 deduced in starburst galaxies by [35] or the translucent sight lines sampled in interstellar C II absorption by [36] with STIS where R_V ranged from 2.6 to 5.1. Examples of where dust grains are not even present or are significantly underabundant include grain disruption in C-shocks with speeds as low as 50 km/s, J-shocks, and the inner regions of the protoplanetary disks or PPDs. The adoption of pre-computed photo-rates may therefore lead to significant uncertainties in molecular abundances in astrochemical models. It is therefore important to return to the computation of the environment-independent property, the photodissociation cross section as obtained here.

Since the important study of molecular optical absorption lines in translucent molecular clouds by [19], a large number of investigations have probed numerous sight lines with *HST*, *FUSE*, *IUE*, and VLT UVES. These observations have detected absorption due to CN as well as H_2, CO, CH, C_2, etc., [**?**, e.g.,]]son07, in our galaxy, in the Magellenic Clouds [37], and beyond. These molecular observations have given new insights into the origin and evolution of a range of astronomical environments. CN itself was apparently first observed in the interstellar medium by [38], but the literature is too vast to be adequately addressed here [**?**, see]for some recent discussions]lis01,lea04. Instead, we discuss three environments where the new CN photodissociation cross sections may have an impact. Due to the various local conditions, photodissociation rates are not provided.

Diffuse and Transluscent Clouds. It is well known that photodissociation due to the interstellar radiation field is a dominant molecular destruction process in diffuse and transluscent clouds. However, extensive observational evidence points to a wide variation in grain properties [**?**, eg.,]]sof05. In fact, the earlier study of [19] found that the observed abundances of CN and C_2 could not be reproduced by their models without significantly adjusting the photodissociation rate. They concluded that either the shape of the UV radiation field was not correct, pointing to variations in dust properties, or that the photodissociation cross sections are unreliable. Further, they performed a parameter study of photo-rates in translucent clouds by adopting various grain models and found that the photodissociation rate for C_2 varied by as much as 2 dex while that for CN had an even larger variation. The finding here that the CN photodissociation cross sections are at least a factor of two smaller than previously given may help to alleviate part of the discrepancy.

Starburst Galaxies. [35] has reviewed the state of knowledge of the dust opacity in nearby galaxies. The existing evidence suggests that the dust content of galaxies depend on the morphology, luminosity, and activity level. She deduced for starbursts the average value of $R_V = 4.05 \pm 0.8$ - far different than the value of 3.1 adopted in the photo-rate calculations of [32]. A large number of molecules are detected in starbursts. For example, [39] observed CN as well as HCN, C_2H, and HOC^+ in the nucleus of M82. The molecules are believed to be formed in a giant PDR with a radiation field of 10^4 Habing units, but PDR models under-predict the abundances of these molecules by a factor of 10. It is then often argued that the molecule abundances can be increased in the models by assuming an enhanced cosmic-ray ionization rate or shocks. However, since the primary destruction process for the neutrals is photodissociation the adoption of pre-computed photo-rates can possibly account for this discrepancy.

Protoplanetary Disks and Circumstellar Shells. A large number of molecules have been observed in the circumstellar shells of asymptotic giant branch (AGB) stars. In particular, refractory molecules have been detected in the well-studied AGB circumstellar environment toward IRC+10216. It was shown by Glassgold and co-workers that the gas-phase chemistry in circumstellar shells is driven by photoprocesssing of "parent" molecules in the inner envelope. However, nearly all models treat photodissociation with pre-computed exponentially-attenuated photo-rates except, for example, those of [40] and [41]. Given that the dust properties and abundances and the radiation field are significantly different from the typical interstellar case [**?**, see, for example]]van06, accurate molecular abundances can only be obtained if local photorates are self-consistently computed. In recent studies of the photochemistry in PPDs, [42] found that the abundances of many molecules, including CN, are sensitive to the adopted photorate, while [43] demonstrated that dust evolution (growth and sedimentation) affect the photorates for important molecules including CN and CS.

In the inner regions of PPDs, as well as in planetary and stellar atmospheres, the gas density may exceed the critical density for most rovibrational levels. In such situations, the level populations can be described by a Boltzmann distribution depending on the gas temperature. The photodissociation cross section can then be obtained, in the so-called local thermodynamic equilibrium (LTE) assumption, by summing over all rovibrationally-resolved cross sections weighted by the LTE population of the levels [**?**, see for example]]miy11. LTE cross sections for all four considered CN electronic transitions have been obtained for temperatures between 500 and 5000 K, with some examples given in Fig. 2.6. The LTE cross sections for 500 K, which are very similar to the cross section from the ground rovibrational level ($v'' = 0, N'' = 0$), are shown in Fig. 2.6a to lie at wavelengths shortward of Lyα and generally reaching their maximum values, except for the $^2\Sigma^+(5) \leftarrow$ X $^2\Sigma^+$ transition, just longward of the Lyman limit. As pointed out by [19], the photodissociation rate of CN is very sensitive to the adopted extinction curve which may vary significantly in this wavelength region. Blackbody radiation intensity curves are also shown for comparison where it is seen that for a gas temperature of 500 K, the CN photodissociation rate will be inefficient for effective stellar temperatures less than 10,000 K, typical of T Tauri stars in circumstellar disks. However, efficient CN photodissociation may result for larger radiation temperatures, but still be negligible for Lyα radiation. Fig. 2.6b displays the LTE cross sections for 3000 K, which is the gas temperature on the disk surface in the PPD models of [44]. As the gas temperature increases, the LTE cross sections shift towards longer wavelengths possibly enhancing the photodissociation rate in most radiation fields. Interesting, a strong resonance develops near Lyα for the $^2\Pi(4) \leftarrow$ X $^2\Sigma^+$ transition.

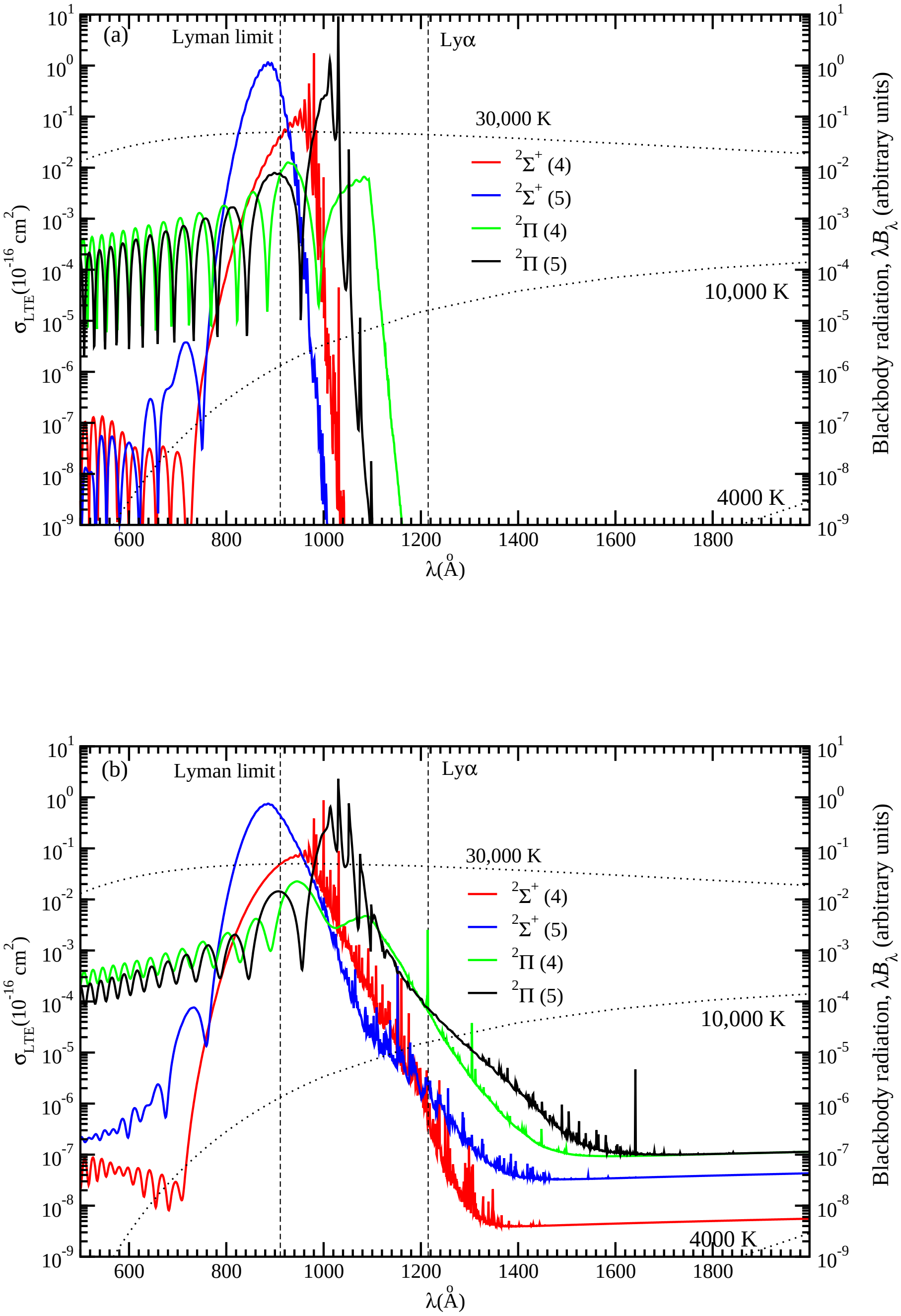

Figure 2.6: CN LTE photodissociation cross sections as a function of wavelength for the transitions $^2\Sigma^+(4) \leftarrow \mathrm{X}\ ^2\Sigma^+$, $^2\Sigma^+(5) \leftarrow \mathrm{X}\ ^2\Sigma^+$, $^2\Pi(4) \leftarrow \mathrm{X}\ ^2\Sigma^+$, and $^2\Pi(5) \leftarrow \mathrm{X}\ ^2\Sigma^+$. (a) 500 K. (b) 3000 K. The dotted curves are for blackbody radiation at the indicated radiation temperatures.

Conclusions

Using a combination of theoretical and experimental data, potential energies and dipole transition moments were constructed and used to perform comprehensive cross section calculations for the photodissociation of CN through the $^2\Sigma^+(4) \leftarrow \mathrm{X}\ ^2\Sigma^+$, $^2\Sigma^+(5) \leftarrow \mathrm{X}\ ^2\Sigma^+$, $^2\Pi(4) \leftarrow \mathrm{X}\ ^2\Sigma^+$, and $^2\Pi(5) \leftarrow \mathrm{X}\ ^2\Sigma^+$ transitions. The partial and LTE cross sections were evaluated for all rovibrational levels $(v''N'')$ of the ground electronic state of CN, X $^2\Sigma^+$, and over a large wavelength range of astrophysical interest. The results will allow for the calculation of reliable CN photodissociation rates for astrophysical environments with varying radiation and dust properties. Further improvements in the CN photodissociation cross sections can be made with refinements in the potential energy and transition moment function calculations.

Chapter 3

Rotational Relaxation of Carbon Dioxide by Collisions with Helium Atoms[1]

Solid CO_2 in interstellar medium, toward several protostars, was first reported in 1989 by [45]. They detected a strong absorption feature at 15.2 μm in the database of the Low Resolution Spectra (LRS) on board the Infrared Astronomical Satellite, $IRAS$, for three sources: AFGL 961 in the Rosette Nebula, AFGL 989 in the Cone Nebula, and AFGL 890. This is associated with the, ν_2, bending mode of the CO_2 ice. They also showed that the abundance of solid CO_2 is almost the same as that for solid CO. In 1996, analyzing data from the Short Wavelength Spectrometer (SWS) on board the Infrared Space Observatory (ISO), [46], reported the detection of solid CO_2 through both its bending and asymmetric stretching, $\nu_3 = 4.27$ μm, modes. The SWS uses a grating of resolving power, $\lambda/\Delta\lambda$, $\sim$ 2000. They detected the solid CO_2 in five infrared sources known as: GL 2591, GL 2136, GL 4176, NGC 7538 IRS9, and Sgr A*. The first four are young stars, while the fifth is a Galactic Center.

---

[1] Based on ' Rotational Relaxation of CO_2 by Collisions with He Atoms', in preparation

They reported a relative abundance of CO_2 to H_2O of $\sim 15\%$. In the same year and using data from the same source, [47], reported detecting gas-phase CO_2, alongside the solid CO_2, in the spectra of the four young stars mentioned earlier. They reported the abundance of gas-phase CO_2 to be less than 5% of that of the solid CO_2 . According to the the same reference, the gas-phase CO_2 abundance is only $\sim 2 \times 10^{-7}$ relative to H_2. CO_2 does not possess a dipole moment. As a result, it can not be detected through millimeter rotational spectra from Earth. Moreover, carbon dioxide is abundant in the Earth's atmosphere. Consequently, detecting its vibrational lines, associated with the bending and stretching modes, must be done from outer space. The technology and the resources to carry spectrometers on satellites was not available until recently. Under conditions in most molecular clouds, molecules exist in their lowest electronic and vibrational state. Moreover, just a few rotational levels are populated. Radiative and collisional transitions between these rotational levels occur with comparable frequency [48]. These transitions determine the level population, and hence the intensity of the observed lines. Radiative and collisional transitions follow different rules. As a result, the rotational levels are not in 'local thermodynamic equilibrium' with either the radiation field or the kinetic temperature [48]. Rates for the radiative transitions are known, however those in the collisional case are not.

In this chapter, the rotational quenching of CO_2 by collisions with He is examined. As 99% of the atoms in the universe are hydrogen and helium, and H_2 is almost 5 times more abundant than He, these two species are frequently used as collision partners. However, collisions with He are in principle easier to treat as helium is an atom whereas H_2 is a molecule. Also, the difference between the two processes, collision with He or H_2, might be insignificant to a first approximation [49].

In this study, carbon dioxide is treated as a rigid linear rotor. For an initial rotational state designated by the quantum number, j, the quenching cross sections, to the state j', resulting from collisions with He atoms were calculated.

3.1 The Multichannel and the Close-coupled Equations

The quantum mechanical treatment of the scattering by a rigid rotor was first formulated by Arthurs and Dalgarno [50] and a detailed account can be found in many books, for example, [51], [52], [53] and [54]. Figure 3.1 illustrates the coordinates relevant to this collision in a space-fixed, SF, coordinate system whose origin is the center of mass of the rotor. Following the discussion in section 1.2, in the center-of-mass frame, the collision between the helium atom and the carbon dioxide molecule is equivalent to the scattering of a particle with mass μ from the interaction potential where μ is the reduced mass of the $He-CO_2$ complex. The internal hamiltonian is just the rotational energy of the rotor, H_{rot}. It is a function of the polar and azimuthal angles, α and β respectively, of the intermolecular axis. The interaction potential is a function of the angle, γ, between the position vector $\vec{r}$ and the intermolecular axis. It also depends on the distance r and it approaches zero as r approaches infinity. γ and r are sometimes called the 'Jacobi coordinates'.

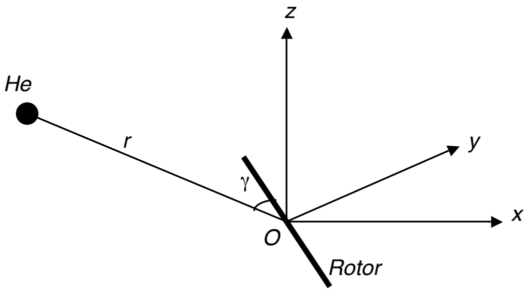

Figure 3.1: Space-fixed, SF, coordinate system for the collision between a He atom and the CO_2 rigid rotor.

The hamiltonian for this system is then,

$$H = H_{rot}(\alpha, \beta) - \frac{\hbar^2}{2\mu}\nabla^2(\vec{r}) + V(r, \gamma), \tag{3.1}$$

If I is the moment of inertia of the rotor, then the hamiltonian for its rotational motion is:

$$\begin{aligned} H_{rot} &= -\frac{\hbar^2}{2I}\left[\frac{1}{\sin\alpha}\frac{\partial}{\partial\alpha}\left(\sin\alpha\frac{\partial}{\partial\alpha}\right) + \frac{1}{\sin^2\alpha}\frac{\partial^2}{\partial\beta^2}\right], \\ H_{rot} &= \frac{\hat{j}^2}{2I}, \end{aligned} \tag{3.2}$$

where $\hat{j}$ is the rotational angular momentum operator. The eigenfunctions of H_{rot} are then the spherical harmonic functions, $Y_{jm_j}(\alpha, \beta)$, where j is the rotational angular momentum quantum number of the rotor and m is its projection on the SF z-axis. The eigenvalues of H_{rot} are:

$$E_j = j(j+1)\frac{\hbar^2}{2I} = j(j+1)B_j, \quad B_j = \frac{\hbar^2}{2I}, \quad and \quad j = 0, 1, 2, \ldots \tag{3.3}$$

The kinetic energy of the relative motion, the second term in equation 3.1, can be separated into an angular part and a translational contribution. The angular part represents the orbital kinetic energy of the helium atom around the center-of-mass of CO_2. It is a function of θ and ϕ, the polar and azimuthal angles, respectively, of the position vector $\vec{r}$. This orbital hamiltonian is identical to H_{rot} in equation 3.2 with α and β replaced by θ and ϕ respectively. Hence, the spherical harmonic functions: $Y_{lm}(\theta, \phi)$ are the eigenfunctions for the orbital hamiltonian with eigenvalues $l(l+1)\hbar^2/2\mu$ where l is the orbital quantum number. The hamiltonian in equation 3.1 can then be written as:

$$H = \frac{\hat{j}^2}{2I} + \frac{\hat{L}^2}{2\mu r^2} - \frac{\hbar^2}{2\mu r}\frac{\partial^2}{\partial r^2}r + V(r, \gamma). \tag{3.4}$$

The spherical harmonic functions constitute a complete orthogonal set, or a basis, so the total wave function can be expanded as:

$$\Psi(\alpha, \beta, \theta, \phi, r) = \frac{1}{r}\sum_{l,m,j,m_j} Y_{lm}(\theta, \phi)Y_{jm_j}(\alpha, \beta)\psi_{lmjm_j}(r). \tag{3.5}$$

$\psi_{lmjm_j}(r)$ is an unknown radial function.

Substituting Ψ as given above in the Schrödinger equation with the hamiltonian in equation 3.4, and applying the orthogonality of the spherical harmonics yields a system of equations, the multichannel equations, which the radial functions $\psi_{lmjm_j}(r)$ must satisfy.

$$\left[\frac{d^2}{dr^2} - \frac{l(l+1)}{r^2} + k_j^2\right]\psi_{lmjm_j}(r) = \frac{2\mu}{\hbar^2}\sum_{l'j'} V_{ljl'j'}(r)\psi_{l'mj'm_{j'}} \tag{3.6}$$

where

$$\begin{aligned} k_j^2 &= 2\mu(E - E_j)/\hbar^2; \\ V_{ljl'j'}(r) &= \int Y^*_{l'm'}(\theta,\phi)Y^*_{j'm'_j}(\alpha,\beta)VY_{lm}(\theta,\phi)Y_{jm_j}(\alpha,\beta)\, d\alpha\, d\beta\, d\theta\, d\phi. \end{aligned} \tag{3.7}$$

Ψ as given above is an eigenfunction of $\hat{j}^2, \hat{l}^2, \hat{j}_z$, and $\hat{l}_z$, but it is not an eigenfunction of the total angular momentum $\hat{J}^2$ or it projection on the z-axis, $\hat{J}_z$. As a result, the potential matrix elements $V_{ljl'j'}$ defined above will couple terms that differ in one or more of the four angular momenta quantum numbers producing a large number of coupled equations that need to be solved simultaneously. Symmetry properties can be utilized to reduce the number of coupled equations.

An important symmetry is the invariance of the Hamiltonian under a rotation of the coordinate system. The leads to the important law of conservation of the total angular momentum, $\boldsymbol{J}=\boldsymbol{j}+\boldsymbol{l}$, of the system. Eigenfunctions of $\hat{J}^2$ can be constructed according to:

$$\begin{gathered} Y^{JM}_{lj}(\theta,\phi,\alpha,\beta) = \sum_{m,m_j} C^{JM}_{lmjm_j} Y_{lm}(\theta,\phi)Y_{jm_j}(\alpha,\beta) \\ J = l+j, l+j-1, \ldots.|l-j|, \\ M = m + m_j. \end{gathered} \tag{3.8}$$

$C^{JM}_{lmjm_j}$ are the *Clebsch − Gordan* coefficients. They are related to Wigner 3j-symbol as:

$$C^{JM}_{lmjm_j} = (-1)^{j-l+M}(2J+1)^{\frac{1}{2}} \begin{pmatrix} j & l & J \\ m_j & m & -M \end{pmatrix} \tag{3.9}$$

The resulting wave function is then:

$$\Psi = \frac{1}{r} \sum_{JMlj} Y^{JM}_{lj}(\theta, \phi, \alpha, \beta)\psi_{JMlj_j}(r) \tag{3.10}$$

Using this Ψ in the Schrödinger equation, then multiplying by the complex conjugate of Y^{JM}_{lj} and integrating over all coordinates except r yields the multichannel equations:

$$\left[\frac{d^2}{dr^2} - \frac{l(l+1)}{r^2} + k_j^2\right]\psi_{JMlj}(r) = \frac{2\mu}{\hbar^2} \sum_{l'j'} V^{JM}_{ljl'j'}\psi_{JMl'j'}(r), \tag{3.11}$$

Here, the potential matrix is block diagonal in J as the collision can not cause a change in the total angular momentum. For each value of J, there are $2J+1$ possible values for M. This produces $2J+1$ blocks of coupled equations for each J. Each block corresponds to one value of M and can be solved independently. As resources needed to solve a system of N coupled equations increases as N^3, the result is considerable savings. The functions in equation 3.8 are also eigenfunctions of the parity operator. They have definite parity, odd or even, under inversion of the coordinates of all particles in the origin of the SF coordinate system. If $\hat{P}$ is the parity operator, then:

$$\begin{aligned} \hat{P}Y^{JM}_{lj}(\theta, \phi, \alpha, \beta) &= Y^{JM}_{lj}(\pi - \theta, \pi + \phi, \pi - \alpha, \pi + \beta) \\ &= (-1)^{j+l}Y^{JM}_{lj}(\theta, \phi, \alpha, \beta). \end{aligned} \tag{3.12}$$

The right hand side of equation 3.11 can be simplified by expanding the potential in angular functions as:

$$V(r,\gamma) = \sum_{\lambda=0}^{\infty} v_\lambda(r) P_\lambda(\cos\gamma), \tag{3.13}$$

where P_λ are the Legendre polynomials. The potential matrix elements can then be written as:

$$V_{ljl'j'}^{JM} = \sum_\lambda v_\lambda(r) \langle jlJM | P_\lambda(\cos\gamma) | j'l'JM \rangle. \tag{3.14}$$

The Symmetry of the carbon dioxide means the potential is invariant when the two oxygen atoms are exchanged. A property shared with homonuclear diatomic molecules. In this case, it is required that:

$$P_\lambda(\cos\gamma) = P_\lambda(\cos(\pi - \gamma)) = P_\lambda(-\cos\gamma). \tag{3.15}$$

Consequently, λ must be even.

The addition theorem for spherical harmonics can be used to write the legendre polynomials in terms of α, β, θ, and ϕ since

$$P_\lambda(\cos\gamma) = \frac{4\pi}{2\lambda+1} \sum_{\nu=-\lambda}^{\lambda} Y_{\lambda\nu}(\alpha,\beta) Y_{\lambda\nu}^*(\theta,\phi). \tag{3.16}$$

The integrals in equation 3.14 can then be evaluated so that the potential matrix elements are given by:

$$\langle jlJM | P_\lambda(\cos\gamma) | j'l'JM \rangle = \sum_\lambda v_\lambda(r) f_\lambda(jl, j'l'; J), \tag{3.17}$$

where $f_\lambda(jl, j'l'; J)$ are often called the 'Percival-Seaton coefficients' as they were first introduced by [55]. They are given by:

$$f_\lambda(jl, j'l'; J) = (-1)^{j+j'-J} \frac{[(2j+1)(2l+1)(2j'+1)(2l'+1)]^{\frac{1}{2}}}{(2\lambda+1)} C_{000}^{jj'\lambda} C_{000}^{ll'\lambda} W(jlj'l'; J\lambda). \tag{3.18}$$

$W(jlj'l';J\lambda)$ are the *Racah* coefficients. They are related to the $6j-$symbol of Wigner as

$$W(jlj'l';J\lambda) = (-1)^{j+l+j'+l'} \begin{Bmatrix} j & l & J \\ l' & j' & \lambda \end{Bmatrix} \tag{3.19}$$

The *Clebsch−Gordan* coefficient, $C_{000}^{jj'\lambda}$, vanishes except when '$j+j'+\lambda'$ is even. Similarly, '$l+l'+\lambda'$, must be even. In this case, one can write:

$$\begin{aligned} (-1)^{j+j'+\lambda+l+l'+\lambda} &= +1 \\ &= (-1)^{j+j'+l+l'}, \quad any \quad \lambda \\ &= (-1)^{j+l}(-1)^{j'+l'} \\ Hence \quad (-1)^{j+l} &= (-1)^{j'+l'} \end{aligned} \tag{3.20}$$

However, $(-1)^{j+l}$, defines the parity of the eigenfunctions of $\hat{J}$, equation 3.12, and hence that of Ψ. The parity then is conserved and transitions occur between states with the same parity.

The symmetry of CO_2 requires λ to be even as explained above. Also, $j+j'+\lambda$ must be even. Then j and j' should both be even or odd and transitions between odd$-j$ and even$-j$ levels do not occur. Hence, the allowed transitions are only those for which Δj is even. This separates each block of coupled equations, with the same J, into two groups: one for even j and the other for odd j. Also, from these two *Clebsch − Gordan*, and that λ must be even, the relation between λ, j, j', l, and l' is given by

$$\lambda = \begin{cases} j+j', j+j'-2, ..., |j-j'|+1 & \text{or} |j-j'|; \\ l+l', l+l'-2, ..., |l-l'|+1 & \text{or} |l-l'|. \end{cases} \tag{3.21}$$

When $\lambda = 0$ then $j' = j$ and $l' = l$. In this case, in the interaction potential expansion in equation 3.13, $P_0(\cos\gamma) = 1$ and $v_0(r)$ contributes to elastic scattering of the He atom from the CO_2 molecule. Potential terms with $\lambda \geq 2$ can produce transitions between different rotational levels according to the triangular inequalities: $|j - j'| \leq \lambda \leq j + j'$. That is $\lambda \geq \Delta j$. Higher values of λ can produce larger transitions Δj. However, the magnitudes of the coefficients, $v_\lambda(r)$ decrease as λ increases. Hence, the probability for transitions with high Δj becomes smaller.

The Multichannel Equations in The Body-Fixed, BF, Frame

The multichannel equations for the collision of an atom and a rigid rotor were derived in a body-fixed frame [56] and it is mentioned here without much detail just for completeness. The origin of the coordinate system is still the center-of-mass. However, the z-axis coincides with the position vector of the atom $\vec{r}$ in figure 3.1. Thus, the z-axis in the BF frame rotates as the collision progresses. The interaction potential is easier to describe, in this frame, as it depends on r and γ. The rotation of the frame, on the other hand, introduces *Coriolis* forces that need to be addressed. A discussion of the advantages of both the SF and the BF coordinates can be found in [57].

3.2 The Cross Section for Rotational Transitions of a Rigid Rotor

In principle, the wave function can be expanded in an infinite number of basis states. In practice, the sum has to be truncated at a finite number N resulting in N coupled multichannel equation called the close-coupled equations. The only variable in equations 3.11 is r. They are solved by numerical integration outwards from $r = 0$, or sufficiently small that the interaction potential is highly repulsive and the wavefunctions for all the channels,

$\psi_{JMl'j'}(r)$, are nearly zero. The integration should be carried out to a value of r where the potential matrix elements, $V^{JM}_{ljl'j'}$, are negligible and equations 3.11 take the free particle form:

$$\left[\frac{d^2}{dr^2} - \frac{l(l+1)}{r^2} + k_j^2\right]\psi_{JMlj}(r) = 0. \tag{3.22}$$

The general solution to these equations is

$$\psi_j(r) = A_j e^{ik_j r} + B_j e^{-ik_j r}, \tag{3.23}$$

where A_j and B_j are called Jost functions and $k_j = \sqrt{2\mu(E-E_j)/\hbar^2}$ are the channel wave numbers. E_j is the energy of the internal state designated by the quantum number j. In our case, the internal states are the rotational states of the rigid rotor. If $E < E_j$ then the channel with energy E_j is closed because the system can not emerge in this state after the collision without violating conservation of energy. On the other hand, if $E > E_j$ then the channel is open and accessible. If the rotor was initially in state j and j' is its final state after the collision, then the solutions given in equation 3.23 should satisfy the asymptotic form:

$$\psi_{j'}(r) \sim \delta_{jj'} e^{-ik_j r} - S_{j'j}\left(\frac{k_j}{k_{j'}}\right)^{\frac{1}{2}} e^{ik_{j'} r} \tag{3.24}$$

Imposing the asymptotic form in 3.24 on the solutions in equation 3.23 relates the Jost functions to the scattering matrix elements S_{ij}. The scattering amplitude is then [50],

$$f(jm_j j'm_{j'};\theta,\phi) = \sum_J \sum_l \sum_{l'} \sum_{m'} \left[\frac{(2l+1)\pi}{k_j k_{j'}}\right]^{1/2} i^{l-l'+1} C^{Jm_j}_{l0jm_j} C^{Jm_j}_{l'm'j'm_{j'}} [S^J_{j'l'jl} - \delta_{ll'}\delta_{jj'}] Y_{l'm'}(\theta,\phi), \tag{3.25}$$

and the differential cross-section is:

$$\sigma(jm_j j'm_{j'};\theta,\phi) = \left(\frac{k_{j'}}{k_j}\right)|f(jm_j j'm_{j'};\theta,\phi)|^2. \tag{3.26}$$

The total cross-section is obtained by integrating the differential cross-section over θ and ϕ. This yields

$$\sigma(jj') = \pi(2j+1)^{-1}k_j^{-2}\sum_{j=0}^{\infty}\sum_{l}\sum_{l'}(2J+1)|S^J_{jlj'l'} - \delta_{jj'}\delta_{ll'}|^2 \tag{3.27}$$

3.3 Calculating the Cross Sections

The close-coupling equations for an atom-rigid rotor system 3.11 were solved using the potential energy surface for the He-CO_2 complex calculated by Ran and Xie [58]. Computations were carried out using the non-reactive molecular scattering package, MOLSCAT [59]. A hybrid log-derivative/Airy propagator [60] was used to solve the close-coupling equations. The modified log-derivative propagator of Manolopoulos [61] and [62] was used from r_{min}, the minimum value of r, to an intermediate value r_{mid} just past the classical turning point. The Airy propagator was then used up to the maximum distance r_{max}. The rotational basis for CO_2 included all open channels and a few closed channels determined by convergence tests. The reduced mass of the $He-CO_2$ complex used was 3.66878 amu. The energies for the CO_2 rotational levels corresponding to $j=0$ up to $j=42$ are shown in Table 3.1.

Symmetry Considerations

CO_2 is a boson since the nuclei have zero spin. In this case, to satisfy Pauli exclusion principle, the total wave function must be symmetric upon exchange of the equivalent nuclei. Carbon dioxide is linear in the ground state and exists in a $^1\Sigma^+$ molecular state. The electronic wave function for the $^1\Sigma^+$ is symmetric. The total wave function can be written as a product of electronic, vibrational, rotational and nuclear wave function. The vibrational wave function is symmetric since it depends on the absolute difference in the coordinates of the atoms. Since the nuclear wave function is symmetric for bosons, the symmetry of the total wave function depends on that of the rotational wave function. As discussed earlier,

Table 3.1: Rotational Levels of CO$_2$

level	energy (cm^{-1})	j	level	energy (cm^{-1})	j
1	0.0000000	0	22	180.2527216	21
2	0.7804375	1	23	197.4166793	22
3	2.3413092	2	24	215.3602649	23
4	4.6826088	3	25	234.0834048	24
5	7.8043267	4	26	253.5860223	25
6	11.7064500	5	27	273.8680374	26
7	16.3889628	6	28	294.9293668	27
8	21.8518459	7	29	316.7699243	28
9	28.0950769	8	30	339.3896201	29
10	35.1186301	9	31	362.7883615	30
11	42.9224768	10	32	386.9660526	31
12	51.5065850	11	33	411.9225941	32
13	60.8709195	12	34	437.6578836	33
14	71.0154419	13	35	464.1718155	34
15	81.9401106	14	36	491.4642812	35
16	93.6448808	15	37	519.5351685	36
17	106.1297045	16	38	548.3843622	37
18	119.3945304	17	39	578.0117441	38
19	133.4393044	18	40	608.4171924	39
20	148.2639686	19	41	639.6005825	40
21	163.8684624	20	42	671.5617863	41
			43	704.3006727	42

for a rigid rotor, the symmetry of the rotational wave function is $(-1)^j$. As a result, only even$-j$ rotational levels in the ground vibrational state of CO_2 are occupied.

The Log Derivative Method

The close-coupled equations are linear with the general form:

$$\psi''(\mathbf{r}) = \mathbf{F}(\mathbf{r})\psi(\mathbf{r}), \tag{3.28}$$

where $\mathbf{F}$ is a symmetric matrix. If all the eigenvalues of $\mathbf{F}$ are negative, then the region is classically allowed for all channels. In this case, integration can be carried out without problems using the Numerov method [22]. On the other hand, if one or more of the eigenvalues of $\mathbf{F}$ is positive, some of the components of ψ increase exponentially as r increases [52]. This makes integrating equation 3.28 difficult. The log derivative method is then better suited to carry out the integration.

The log derivative of ψ is defined as,

$$\mathbf{X} = \psi' \psi^{\mathbf{-1}}. \tag{3.29}$$

The derivative of which is given by:

$$\mathbf{X'} = \psi'' \psi^{\mathbf{-1}} - \psi' \psi^{\mathbf{-1}} \psi' \psi^{\mathbf{-1}}. \tag{3.30}$$

The second-order equations can then be transformed to the first-order non-linear equations

$$\mathbf{X'} = \mathbf{F} - \mathbf{X^2} \tag{3.31}$$

Johnson [62] derived an algorithm to integrate this equation.

3.4 Results: Cross Sections and Rate Coefficients

Figures 3.2-3.5 show results for the quenching of CO_2 rotational states designated by j =10, 20, 30, and 40 to all possible lower energy states j'. The top figure shows the state-to-state cross sections, while the figures at the bottom show the corresponding rate coefficient. The cross sections have similar features in general. They are dominated by the $\Delta j = j' - j = -2$ transition. That is, transitions to the next immediate lower state have the largest probability while transitions to states with lower j', that is Δj= -4, -6,... have smaller cross sections. The cross sections for a given transition generally decrease with increasing collision energy. In other words, the cross sections follow the exponential energy-gap law [63] in which the probability for energy transfer decreases exponentially with the final kinetic energy available in the collision. The lines also do not cross. Resonance features are absent in accordance with an earlier study [64]. An increase in the cross sections, though, can be seen at about 30 cm^{-1} for j=10. A more pronounced increase can be seen at around 100 cm^{-1} for the j=20, 30, and 40. In the limit as the collision's energy approaches zero, where the s-wave scattering is dominant, the cross sections vary as $\sim v^{-1}$ in agreement with the Wigner threshold laws [4].

The rate coefficients were obtained by averaging the cross sections over the Maxwell-Boltzmann distribution of relative velocities. The results show the state-to-state rate coefficient. They tend to a constant at very low temperature in agreement with the expected Wigner threshold behavior. However, the rate coefficient increases rapidly at $\sim$ 10 to $\sim$ 500 K before approaching a constant in the limit of high temperature considered here. This behavior is more pronounced the higher the initial rotational state, j, of the CO_2 molecule.

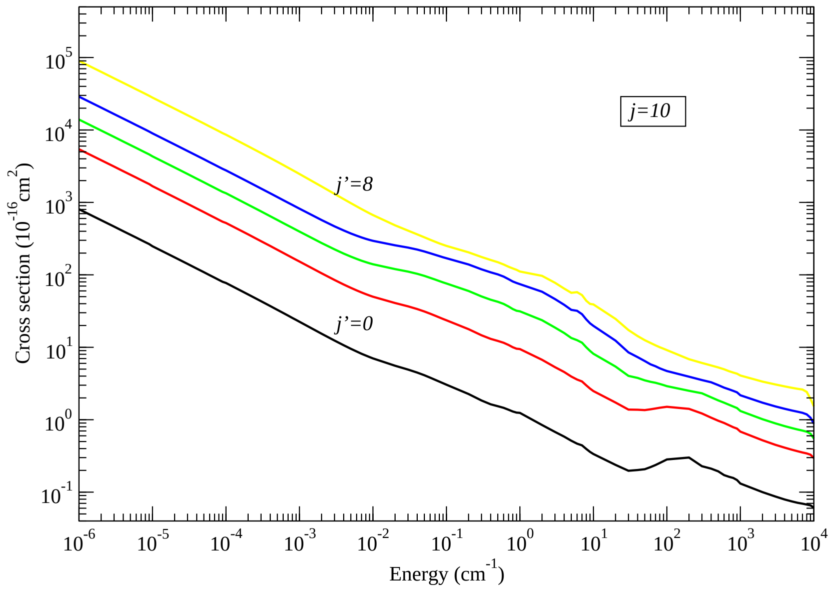

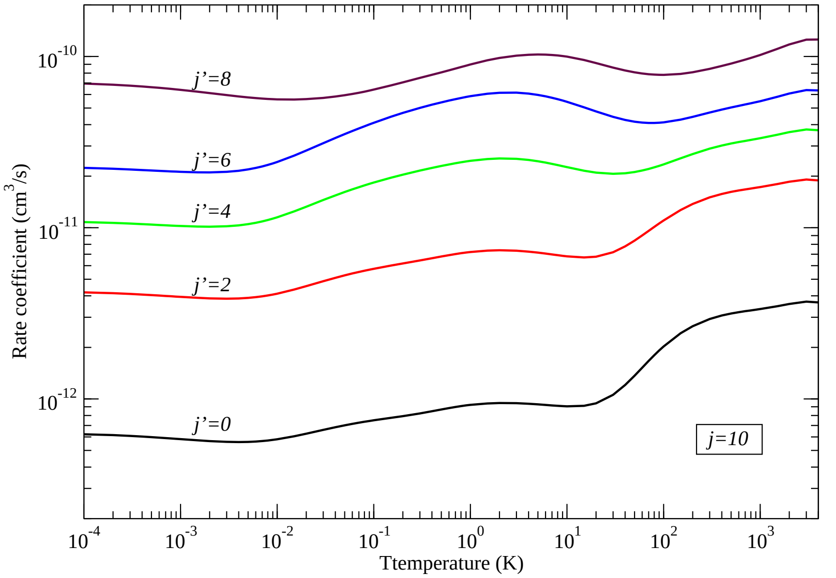

Figure 3.2: CO_2 quenching, from j=10 to all possible j', due to collisions with He. Top: State-to-state cross sections. Bottom: State-to-state rate coefficients as a function of temperature.

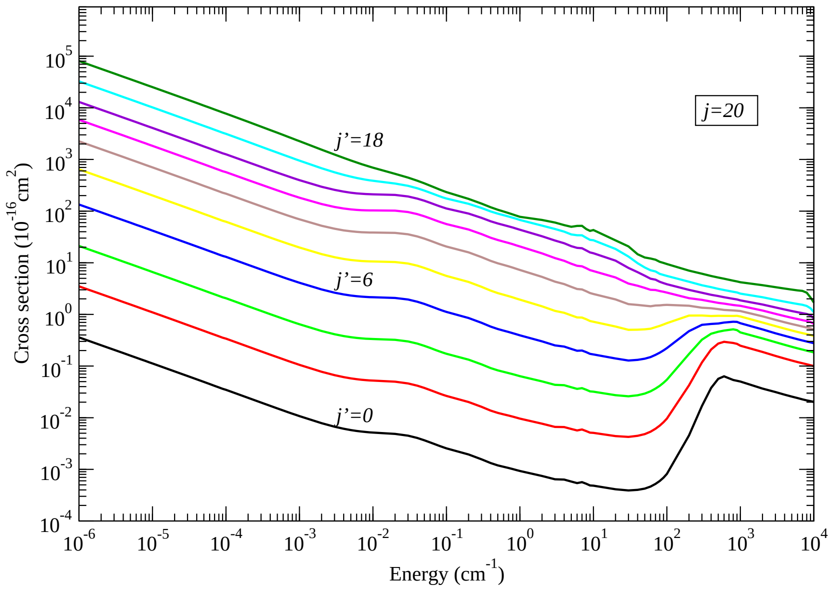

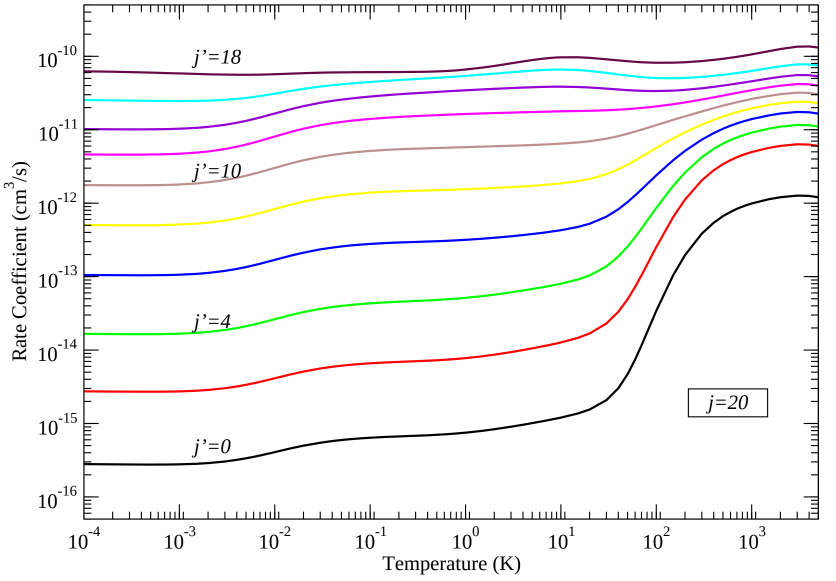

Figure 3.3: CO_2 quenching, from j=20 to all possible j', due to collisions with He. Top: State-to-state cross sections. Bottom: State-to-state rate coefficients as a function of temperature.

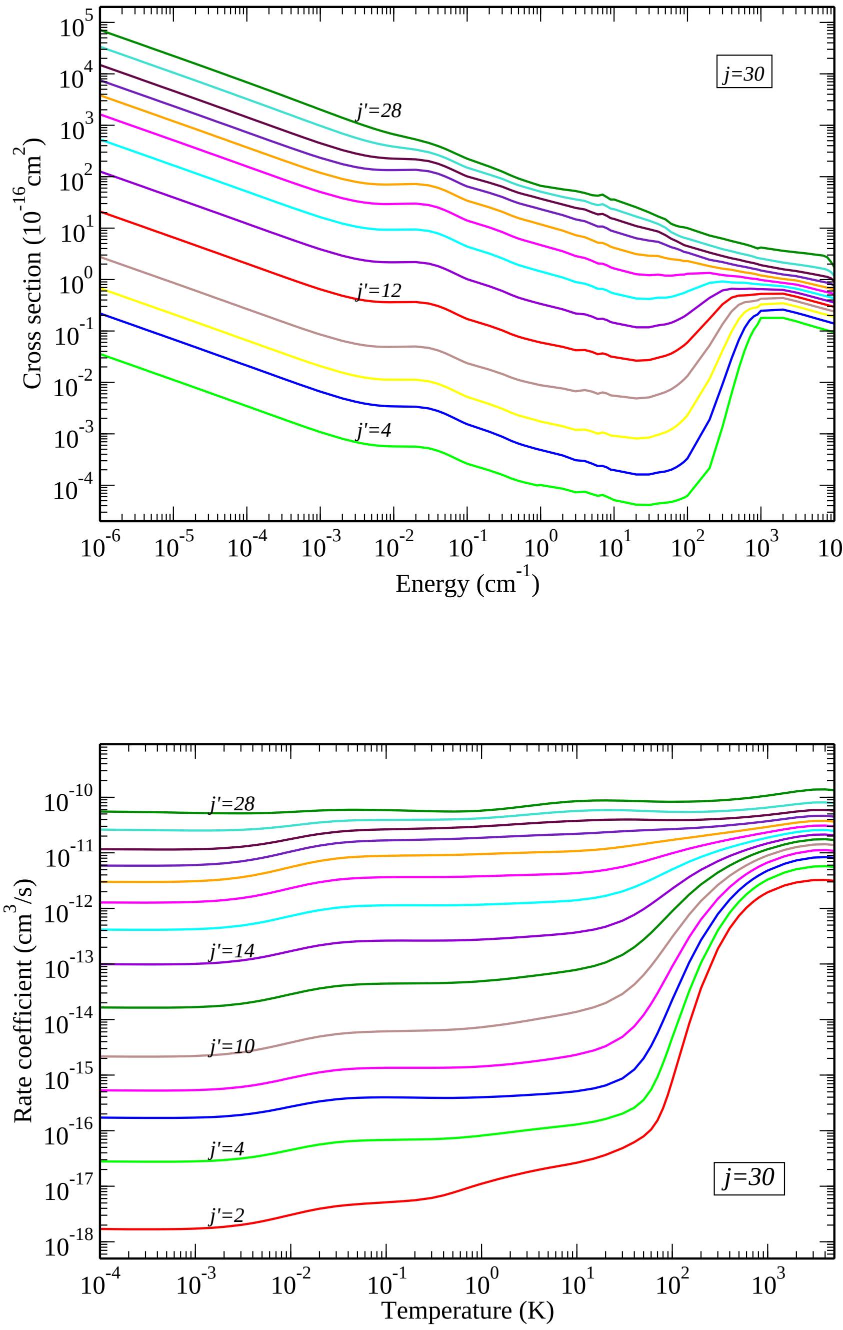

Figure 3.4: CO_2 quenching, from j=30 to all possible j', due to collisions with He. Top: State-to-state cross sections. Bottom: State-to-state rate coefficients as a function of temperature.

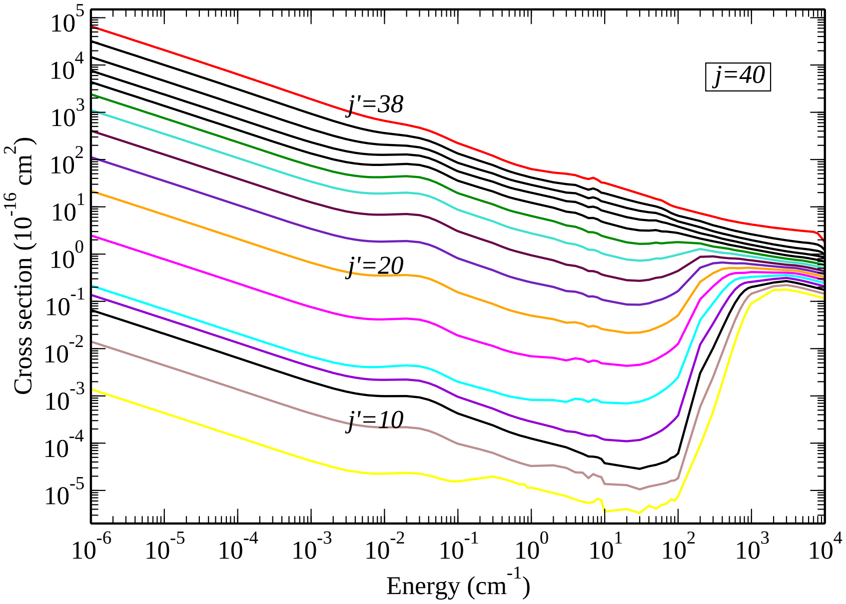

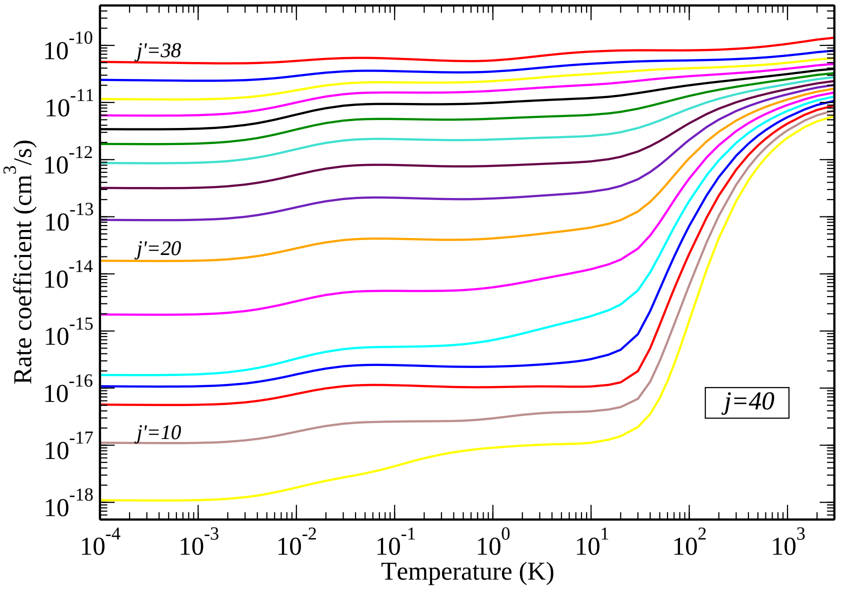

Figure 3.5: CO_2 quenching, from j=40 to all possible j', due to collisions with He. Top: State-to-state cross sections. Bottom: State-to-state rate coefficients as a function of temperature.

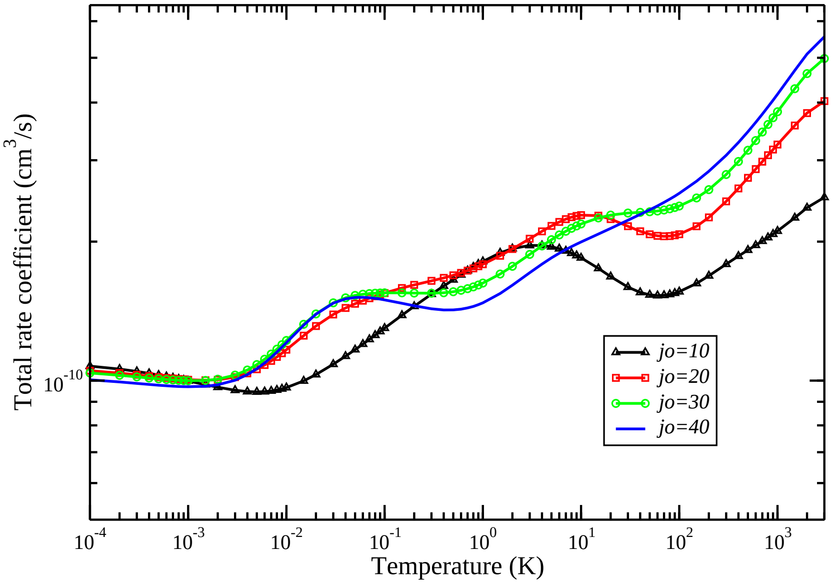

Figure 3.6: CO_2 Total rate coefficients for quenching from j =10, 20, 30, and 40 due to collisions with He as a function of temperature.

Conclusions

The rotational quenching of CO_2 by collisions with He was studied. CO_2 was treated as a rigid rotor in the first ground state. If CO_2 is initially in the rotational state specified by the rotational quantum number j_o, cross sections for transitions to all possible lower$-j$ rotational states, for a wide range of relative collision energy, were calculated based on the theoretical frame work of [50]. Cross sections for transitions to higher$-j$ rotational states can be obtained through detailed-balance. Cross sections are dominated by the $\Delta j = j' - j = -2$ transition. They follow the exponential energy-gap law [63], and they agree with the Wigner threshold laws [4]. Resonance features are absent in accordance with an earlier study [64]. State-to-state rate coefficients were calculated. The rate coefficient behavior is more pronounced for transitions with large Δj. They increase steadily for low temperature, but sharply in the high temperature limit as such transitions become more probable. Rate coefficients for the $\Delta j = j' - j = -2$ transition are almost constant.

Chapter 4

Quenching of Rotationally Excited CO_2 at Ultra Cold Temperatures[1]

4.1 Introduction

The cooling and trapping of molecules produces unique environments that can be used to study molecular interactions at very low and even ultracold temperatures. The availability of such cold molecular systems can be used to investigate a variety of phenomena including fundamental constant variation, quantum computing algorithms, strongly-correlated systems [65, 66], inelastic collisions, cold chemistry [67, 68], and a host of other forefront areas in contemporary physics [69]. A variety of approaches have been developed to produce translationally cold molecules [70], but a major workhorse is the helium-buffer gas method, where the molecules are slowed down through elastic collisions with cryogenically cold He atoms [71].

Over the past decade, there has been an increasing interest in generating molecules in high rotational levels, so-called super rotors [72, 73, 74]. An interesting aspect of super rotors

---

[1] Based on W. H. al-Qady, R. C. Forrey, B. H. Yang, P. C. Stancil and N. Balakrishnan, Phys. Rev. A **81**, 014701 (2011). Copyright (2011) by the American Physical Society. Reprinted with permission of publisher.

is their prospect for unique properties at very low temperature. Forrey [75, 76] proposed that super rotors could be translationally cooled and trapped, as ultracold molecular rotational quenching rates generally decrease with increasing rotational excitation. If rovibrational quenching is also small, as is often the case for specific rotational levels at temperatures accessible to helium buffer-gas methods, then the super rotors would be stable against collision. Here, we demonstrate the feasibility of producing cold super rotors by exploring the dependence of scattering properties with rotational excitation for inelastic He-CO_2 interactions.

4.2 The Complex Scattering Length

At very low energies, the scattering is dominated by the s-wave ($l = 0$) term. In this regime, the scattering can be described by the complex scattering length, $a = \alpha - i\beta$ [77]. β is derived from the inelastic cross section [78] and gives a measure of the total decay probability of an internal excited state. For an initial state with vibrational and rotational quantum numbers v and j, the imaginary part of the scattering length β_{vj} in the limit of zero initial kinetic energy is given by

$$\beta_{vj} = k\sigma_{vj}^{\mathrm{in}}/4\pi, \tag{4.1}$$

where k is the initial wave vector and $\sigma_{vj}^{\mathrm{in}}$ the sum of the inelastic cross sections of all open channels [78]. In the limit $k \to 0$, the relation between the elastic cross section $\sigma_{vj}^{\mathrm{el}}$ and the complex scattering length a_{vj} is given by [78]

$$\sigma_{vj}^{\mathrm{el}} = 4\pi(\alpha_{vj}^2 + \beta_{vj}^2) = 4\pi|a_{vj}|^2, \tag{4.2}$$

from which the magnitude of the real part of the scattering length is given by

$$|\alpha_{vj}| = \sqrt{\sigma_{vj}^{\mathrm{el}}/4\pi - \beta_{vj}^2}, \tag{4.3}$$

while the sign of α_{vj} is determined from the sign of the phase shift. Application of the complex scattering length formalism to low-lying rotational levels of the He-CO$_2$ system, and other linear and non-linear molecules, was given in [79].

4.3 Results and Discussion

In Figure 4.1, the real part, α, and the imaginary part, β of the scattering lengths for the ultracold collision energy of 10^{-6} cm^{-1} are presented. Results are shown for the CC and CS methods as the CS approximation is more computationally efficient for larger j. As β depends only on the inelastic cross sections, it is a measure of the quenching of j. Similarly, an increase in α, indicates an increase in the elastic scattering. For $j \leq$16, β is larger than α indicating that rotational quenching will be very efficient. As j increases, α increases rapidly plateauing for $j \gtrsim 120$. On the other hand, β decreases slowly with j, but then drops relatively rapidly for $j \gtrsim 80$. This trend is alternatively shown in Figure 4.2 for the ratio β/α where it is noted that the differences between results obtained with the CC and CS methods are largely removed.

In cooling and trapping experiments, inelastic quenching cross sections need to be small compared to the elastic cross sections to avoid trap loss. A *figure-of-merit* for the ability to trap a species is given by the ratio of the elastic to inelastic cross sections, $\sigma^{\mathrm{el}}/\sigma^{\mathrm{in}}$, which is related to the components of the complex scattering length by

$$\frac{\sigma^{\mathrm{el}}}{\sigma^{\mathrm{in}}} = \frac{k(\alpha^2 + \beta^2)}{\beta}. \tag{4.4}$$

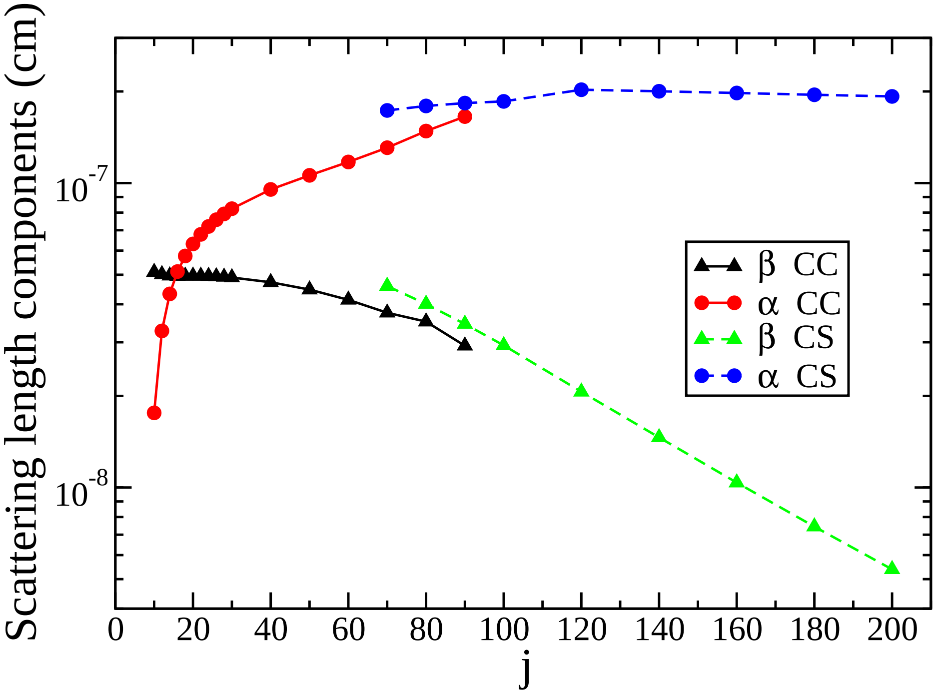

Figure 4.1: Real and imaginary parts, α and β, respectively, of the scattering length as a function of the rotational level j. All calculations were performed at 10^{-6} cm^{-1}.

In the limit of $\alpha >> \beta$, as shown for large j in Figures 4.1 and 4.2,

$$\frac{\sigma^{\mathrm{el}}}{\sigma^{\mathrm{in}}} \approx \frac{\alpha}{\beta} k\alpha. \tag{4.5}$$

In the zero-temperature limit, α and β are constant for a given j, hence their utility. As the energy (or k) increases, but still within the Wigner regime, the *figure-of-merit* improves as it is approximately proportional to k. As an illustration, we show in Figure 4.3 the elastic and inelastic quenching cross sections, but for the slightly higher energy of 10^{-4} cm^{-1}. Trends similar to the scattering lengths are evident. The ratio β/α (not shown) is nearly identical

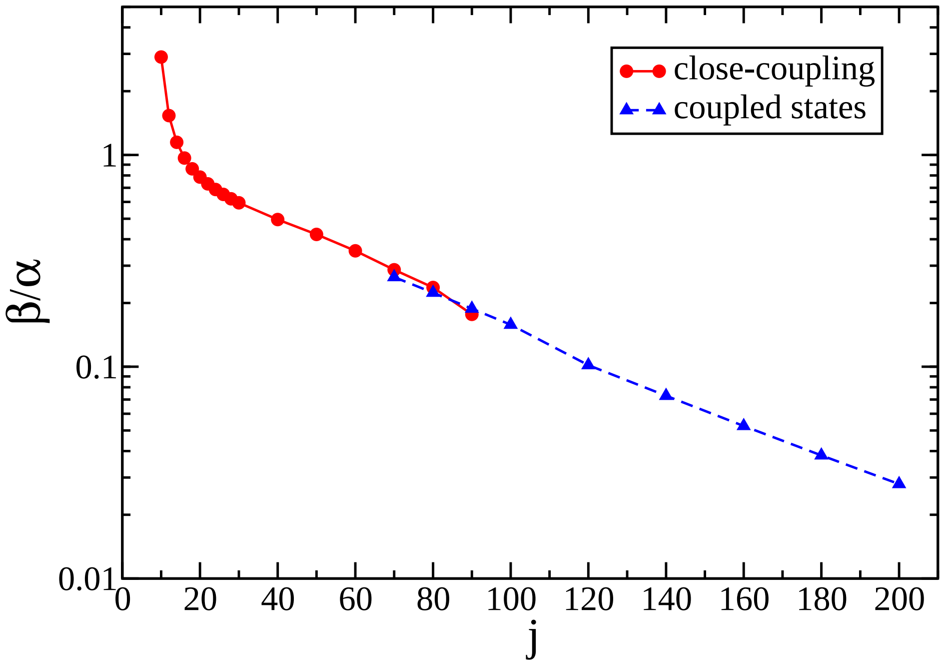

Figure 4.2: Ratio of the imaginary part β to the real part α of the scattering length for ^{4}He collisions with CO$_2$ as a function of the rotational level j. All calculations were performed at 10^{-6} cm^{-1}.

to that given in Figure 4.2. For large j, rotational quenching is dominated by $\Delta j = -2$ transitions, which becomes a factor of $\sim$5 smaller than the elastic cross section for $j = 200$.

The gas temperatures for He buffer-gas cooling are typically beyond the range of the Wigner regime so that equations (4.4) and (4.5) are no longer valid. As the collision energy increases to the He buffer-gas region, the number of required partial waves also increases. The computational time for scattering calculations within the CS approximation scales as $\propto j_{\rm max}^4/2$ per partial wave, where $j_{\rm max}$ is the largest rotational state included in the basis. At the present, computations of elastic and quenching cross sections up to 1000 cm^{-1} have only been completed for $j = 40$. For example, the total number of partial waves needed to secure

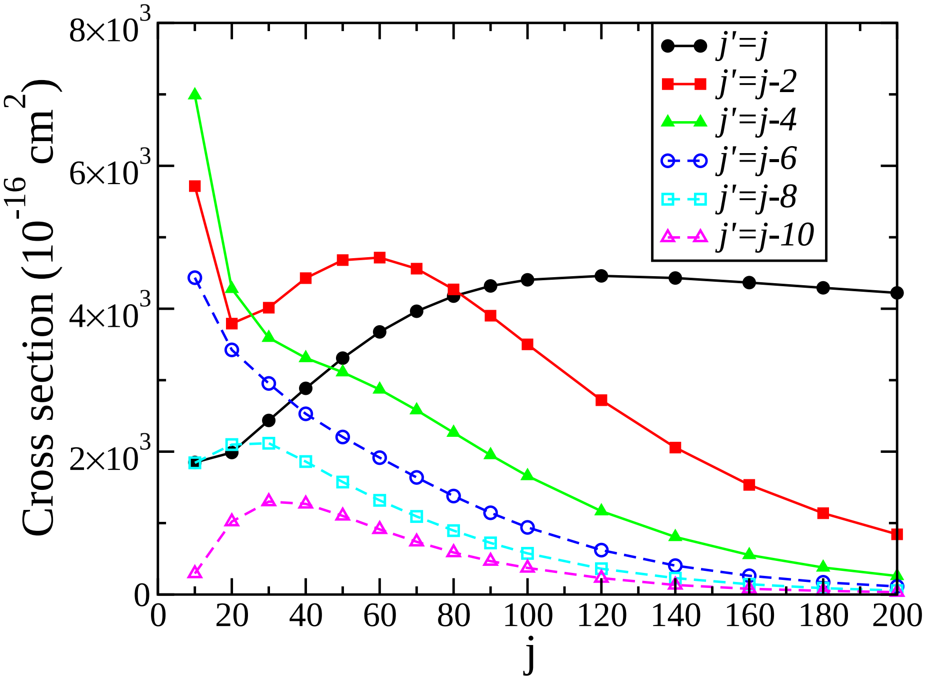

Figure 4.3: Elastic and final-state j' resolved cross sections as a function of initial rotational level j for a collision energy of 10^{-4} cm^{-1} obtained with the CS approximation for ^{4}He-CO$_2$.

convergence for $j = 40$ at a collision energy of 1000 cm^{-1} was 50. We therefore estimate by extrapolation that the figure-of-merit will be large for He-CO$_2$($j = 200$) at 0.5 K.

To illustrate this, the elastic and total inelastic cross sections for j = 10, 20, 24, 30, and 40 are shown in Figure 4.4 from 10^{-2} to 10 cm^{-1}. The typical Wigner threshold behavior of the cross sections are clearly evident at low energy. The cross sections typically depart from the Wigner regime near the collision energy where the total inelastic cross section is equal to that of the elastic cross section. Figure 4.5 shows that the crossing energy is a monotonically decreasing function of j. By j = 70, the crossing energy is significantly smaller than the He cryogenic temperature. A simple extrapolation of Figure 4.5 suggests that the crossing energy will be smaller than 10^{-3} cm^{-1} for $j \sim 200$.

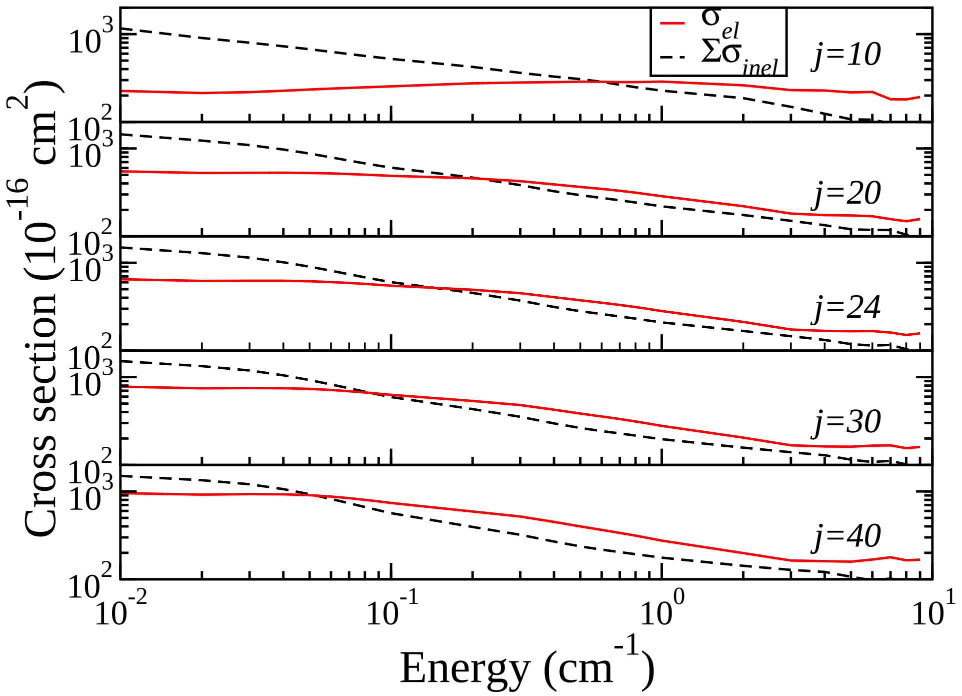

Figure 4.4: Elastic cross section and total inelastic cross section as a function of energy for He collisions with CO_2 and various j.

The ratio of the elastic to total inelastic cross section, or figure of merit, is displayed in Figure 4.6 for various collision temperatures in the cold regime as a function of j. The ratio is seen to increase with j and with temperature up to 1 K. Simple extrapolation to $j \sim 200$ suggests a figure of merit of ∼10, which is encouraging for possible cooling and trapping experiments, if such highly excited states could be created.

To create super rotors, Karczmarek *et al.* [72] proposed that two circularly-polarized laser fields could be used to spin diatoms up to very high rotational levels. This so-called optical centrifuge approach was experimentally demonstrated for Cl_2 by Villeneuve *et al.* [74], reaching a maximum rotational angular momentum of $j \sim 420$. Preliminary experiments on

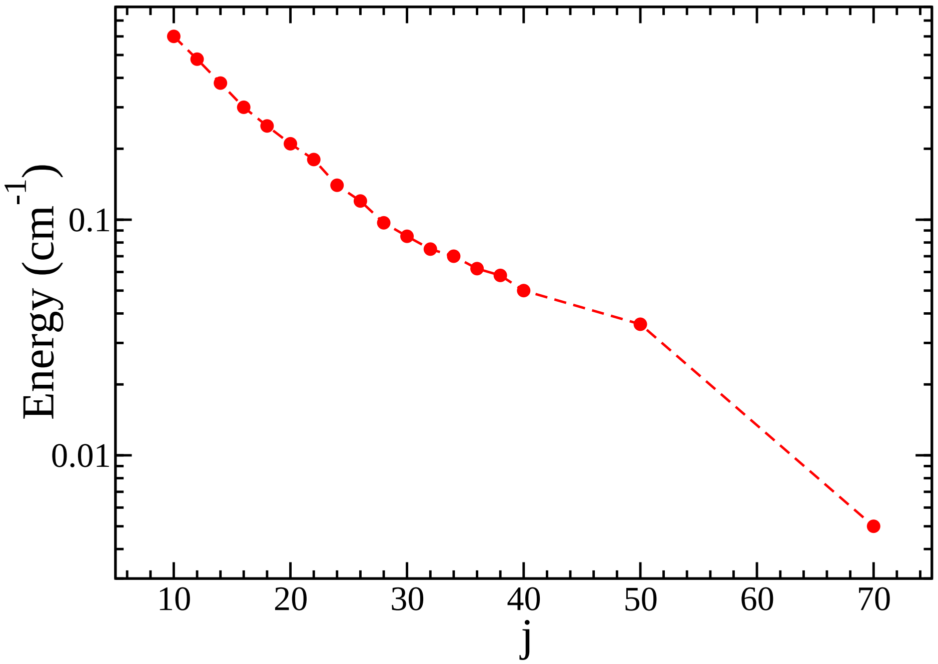

Figure 4.5: The energy where the elastic cross section is equal to the total inelastic cross section as a function of the rotational level j.

O_2 and CS_2 gave similar results [74]. The original experiments were done in a supersonic molecular beam containing the molecules to be spun-up. If a surface was inserted into the beam just downstream from the laser, the super rotors would hit the surface with the jet's velocity, which would be about 700 m/s [80].

A related proposal was given by Li *et al.* [73], but unlike the work of Refs. [72, 74] which results in a distribution of rotational levels, their scheme would produce molecules in a single, selected j level. Numerical simulations found that Li_2 could be excited to $j > 115$ [73]. Following on earlier studies of CO_2 collisions with highly vibrationally excited azulene [81], Mullin *et al.* [82] applied the optical centrifuge approach to room-temperature CO_2

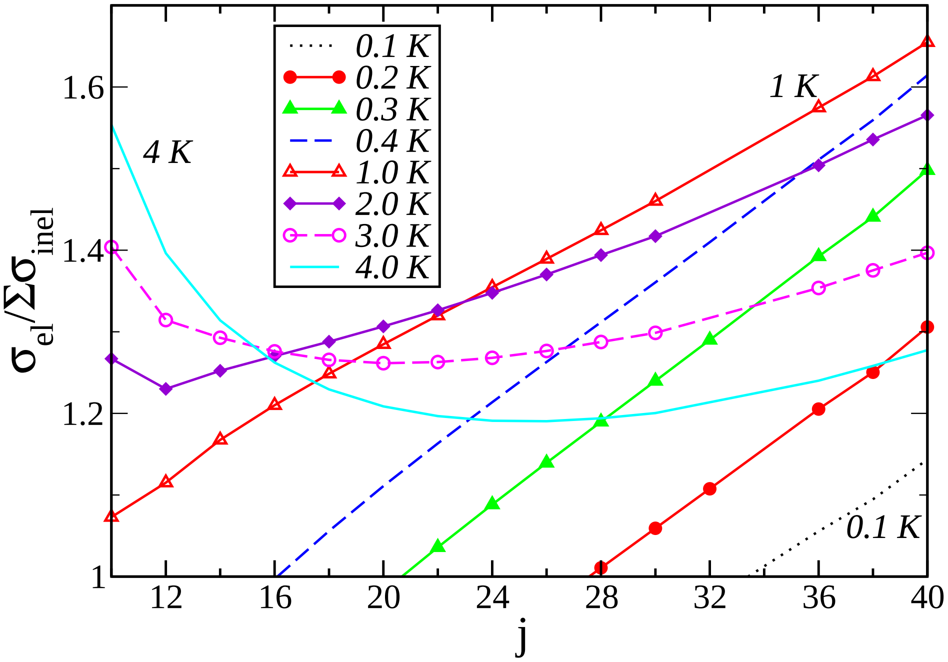

Figure 4.6: The ratio of the elastic cross section to the total inelastic cross section at different temperatures as a function of j.

obtaining excitations to $j \sim 200$.

The experiments described above produce molecular super rotors that are also translationally hot. These molecules are generally extremely fragile against collisions due to efficient quasiresonant vibration-rotation (QRVR) energy transfer. If the super rotors are produced from a translationally cold gas, however, the QRVR transitions are energetically closed and the molecules are stable against collision [75, 76].

Merging these two concepts, we propose a scheme to produce rotationally hot, but translationally cold molecules which could be readily realized for the explicit case of carbon dioxide by combining an optical centrifuge in a helium buffer-gas cell. A possible scheme would be:

i) Introduce room-temperature CO_2 into the gas cell with cryogenic ^{4}He or ^{3}He. CO_2 would be rapidly translationally cooled through elastic collisions and rotationally cooled to $j = 0$ via inelastic collisions (see Fig. 4.4, for example). ii) With ultrafast laser pulses, spin-up the molecules to high rotational levels. Elastic collisions with He would maintain low translational energies for the high j levels, while a limited fraction would be lost due to inefficient inelastic collisions. iii) Both He and CO_2 would then be allowed to exit the cell via a small hole [83], creating a beam of CO_2 super rotors that is considerably slower than what would be produced by a supersonic jet. These super rotors would be much less fragile against collision due to the closed QRVR transitions. The rotational level distribution of the beam would be highly stable as CO_2 lacks a dipole moment.

An optical centrifuge generally produces a range of j and m_j in accordance with Raman selection rules. If the molecules are initially in the $j = 0$ state, then the distribution of super rotors would include only even j and m_j. Further selection of m_j levels could be obtained through magnetic Feshbach tuning of β before ejection of the beam. A variety of novel low temperature experiments could then be envisioned including collisions with electrons, photons, atoms, molecules, and surfaces which may reveal unique properties (see also [74]). While Li *et al.* did mention the possibility of using cold molecules in their super rotor scheme, we demonstrate with accurate scattering calculations the feasibility of our approach here with current available technology.

Finally, the scheme could be extended to highly vibrationally excited states for specific rotational levels which allow QRVR transitions at normal temperatures, but are energetically closed as the temperature is lowered to that in the He buffer gas cell. The availability of downward vibrational transitions generally increases the rotational state selectivity of collisionally-stable super rotors.

Conclusions

Complex scattering lengths and elastic and inelastic rotational quenching cross sections have been computed for carbon dioxide, with rotational excitation j as high as 200, due to ultracold ^{4}He collisions. It is predicted that the ratio of the elastic to inelastic cross section, or figure-of-merit, is sufficiently large that highly rotationally excited CO_2 could be a viable candidate for cooling and trapping. A novel experiment combining a He buffer gas cell with an optical centrifuge is proposed as a means of producing rotationally hot, but translationally cold CO_2. A high-flux beam of cold CO_2 super rotors could be created and used for a variety of scattering experiments.

Chapter 5

Dynamics of Excited Helium Scattering by Helium

5.1 Introduction

Collisions between electronically excited atoms and molecules are important in the study of energy transfer mechanisms in shock waves, explosions, and electrical discharge among others. In this case, a transfer of excitation from one system to the other is possible. That is: $A^* + B \to A + B^*$.

For a given species, when excited atoms are scattered by ground state atoms of the same species, the excitation transfer does not result in a change in the relative energy, so it is elastic in this sence. However, since the internal states of the two colliding systems were exchanged, i.e., $A + A^* \to A^* + A$, it is not pure elastic. It is called exact-resonance excitation transfer collision.

Helium has received special interest. Most monatomic gases will condense before reaching low enough temperatures for quantal effects to manifest, however, these effects are obvious on the diffusion and viscosity of helium at temperature below 50^o K.

5.2 Collisions between Metastable Helium Atoms and Normal Helium Atoms

In collisions between similar atoms, attention must be given to the fact that the nuclei are identical. When excited helium atoms are scattered by their normal counterparts, for example, it is impossible to distinguish between the excited atoms in the original beam and the excited atoms resulting from resonant excitation transfer. As a result, the cross section for a given direction is the sum of the cross section in that direction and the cross section in the opposite direction. The quantum treatment for such collisions was developed by Massey and Smith [84]. It was applied to the case of helium, collisions between metastable and normal atoms, by Buckingham and Dalgarno [85, 86].

For slow collisions where the relative velocity is much smaller than the orbital velocity of the electrons, the total wave function, in the adiabatic representation, equation 1.16, can be written as:

$$\Psi(\vec{r},\vec{\rho}) = \sum_j \psi_j(\vec{r})\chi(s_1,s_2)\phi_j(\vec{r},\vec{\rho}), \tag{5.1}$$

where the nuclear spin function $\chi(s_1,s_2)$ was added. The subscripts 1 and 2 stand for the two atoms involved.

To solve the scattering problem with Ψ as given above, the radial nuclear function is expanded in terms of partial waves as

$$\psi_j(\vec{r}) = \sum_{l=0}^{\infty} i^l(2l+1)\zeta_l(r)P_l(\hat{r}\cdot\hat{k}). \tag{5.2}$$

Since the ^4He nuclei have zero spin, Pauli principle requires the total wave function to be symmetric with respect to interchange of the nuclei, $\vec{r}_1 \rightleftharpoons \vec{r}_2$. This is equivalent to $\vec{r} \rightleftharpoons -\vec{r}$.

Under this transformation, the legendre polynomials P_l behave as

$$P_l(\hat{r} \cdot \hat{k}) = (-1)^l P_l(-\hat{r} \cdot \hat{k}). \tag{5.3}$$

$\psi_j(\vec{r})$ can then be written as the sum of an even part, e, and an odd part, o [87] as

$$\begin{aligned} \psi_j(\vec{r}) &= \psi_j^e(\vec{r}) + \psi_j^o(\vec{r}) \qquad (5.4) \\ &= \sum_{l=even} i^l(2l+1)\zeta_l(r)P_l(\hat{r} \cdot \hat{k}) + \sum_{l=odd} i^l(2l+1)\zeta_l(r)P_l(\hat{r} \cdot \hat{k}). \end{aligned}$$

For the case of collision between two helium atoms, one in its ground state, $He(1^1S)$, and the other in the first excited state, $He^*(1s2s, 2^3S)$

$$He(1^1S) + He^*(1s2s, 2^3S) \rightarrow He^*(1s2s, 2^3S) + He(1^1S). \tag{5.5}$$

The molecule He_2 can form in the Σ_g^+ or the Σ_u^+ state with equal probabilities. The electronic wave function is symmetric for the *gerade*, g, state when $\vec{\rho} \rightleftharpoons -\vec{\rho}$. $\phi_j(\vec{r}, \vec{\rho})$ is not symmetric for the *ungerade*, u, state. However, upon nuclear inversion

$$\phi_j(\vec{r}, x_i, y_i, z_i) = \phi_j(\vec{r}, -x_i, y_i, -z_i), \tag{5.6}$$

where the $z - axis$ were taken along the nuclear axis. Reflection of the coordinates for all electrons in a plane containing the internuclear axis, leaves the electronic wave function unchanged for the Σ^+ states. For the Σ^- states, the effect is multiplying ϕ by -1. This property, combined with equation 5.6 makes the electronic wave function symmetric upon inversion of nuclei for the Σ_g^+, and Σ_u^- states, but antisymmetric for the Σ_g^-, and Σ_u^+ states.

The total, symmetric, wave function can then be written as:

$$\Psi(\vec{r},\vec{\rho}) = \psi_g(\vec{r})\phi_g(\vec{r},\vec{\rho}) + \psi_u(\vec{r})\phi_u(\vec{r},\vec{\rho}), \tag{5.7}$$

where $\phi_g(\vec{r},\vec{\rho})$ and $\phi_u(\vec{r},\vec{\rho})$ are the wave functions associated with Σ_g^+ and Σ_u^- states respectively.

The scattering problem is solved with the asymptotic form of Ψ as a boundary condition. The nuclear wave function in the asymptotic region is:

$$\psi_g(\vec{r}) \rightarrow_{r\rightarrow\infty} \left[e^{ikz} + \frac{e^{ikr}}{r} f^g\right], \tag{5.8}$$

where e^{ikz} represents the incident plane wave, and f^g is the scattering amplitude given by

$$f^g = \frac{1}{2ik} \sum_{l=even} (2l+1)(e^{2i\delta_l - 1}) P_l(\cos\theta), \tag{5.9}$$

where δ_l is the phase shift. For $\psi_u(\vec{r})$, the sum is over the odd partial waves and the corresponding scattering amplitude is f^u.

According to Massey and Smith [84], for bosons, the scattered amplitude is:

$$f(\theta) = \frac{1}{2}\left[f_g(\theta) + f_g(\pi-\theta) + f_u(\theta) - f_u(\pi-\theta)\right]. \tag{5.10}$$

Since $f_g(\theta)$ and $f_u(\theta)$ are significant only for small angles θ, $f_{g,u}(\theta)$ and $f_{g,u}(\pi-\theta)$ do not overlap. The scattered intensity of the excited atoms per unit solid angle is then:

$$|f(\theta)|^2 = \frac{1}{4}\left[|f_g(\theta) + f_u(\theta)|^2 + |f_g(\pi-\theta) - f_u(\pi-\theta)|^2\right]. \tag{5.11}$$

The first term is due to direct elastic scattering of the excited atoms, while the second is related to elastic scattering with excitation transfer. There is no significant direct elastic scattering at large angles except near resonance. Consequently, excited atoms scattered at large angles are ground state atoms which become excited by the collision.

Buckingham and Dalgarno [85, 86] derived the following expressions for the total elastic cross section, the diffusion and the excitation transfer cross section for the process in 5.5.

$$\begin{aligned}\sigma_{tot} &= 2\pi \int_0^{\pi} |f(\theta)|^2 \sin\theta \, d\theta, \\ &= \frac{4\pi}{k^2} \sum_l (2l+1) \sin^2 \delta_l. \end{aligned} \tag{5.12}$$

Diffusion is reduced by backward scattering, that is collisions through an angle $\theta \simeq 180^o$. Hence, the diffusion cross section is defined as

$$\begin{aligned}\sigma_d &= 2\pi \int_0^{\pi} (1 - \cos\theta) |f(\theta)|^2 \sin\theta \, d\theta, \\ &= \frac{4\pi}{k^2} \sum_l (l+1) \sin^2(\delta_{l+1} - \delta_l). \end{aligned} \tag{5.13}$$

and

$$\begin{aligned}\sigma_{tr} &= \frac{\pi}{2} \int_0^{\pi} |f_g(\theta) - f_u(\theta)|^2 \sin\theta \, d\theta, \\ &= \frac{\pi}{k^2} \sum_l (2l+1) \sin^2(\delta_l^g - \delta_l^u). \end{aligned} \tag{5.14}$$

where $k^2 = 2\mu E$, and δ_l is equal to the phase shift associated with the g state when l is even and for odd partial waves, it is equal to the phase shift associated with the u state.

The Potential Energy Surface

New potential energy curves of He_2 prepared by Buenker et al. [88] were used. These curves are shown in figure 5.1. The potential energy was calculated using the multi-reference single- and double-excitation configuration interaction (MRD-CI) method [89, 90]. Self-consistent field (SCF) calculation were utilized to obtain orthonormal basis set of molecular orbits. Those, in turn, were used to construct the many-electron functions which are the basis set for the MRD-CI calculations for both ground and excited electronic states.

The equilibrium separation for the He_2 molecule is around $\sim 2a_o$. In the metastable state, $c^3\Sigma_g^+$ has an attractive well ~ 0.627 eV deep, and a repulsive hump of ~ 0.289 eV at a nuclear separation of $\sim 3.6a_o$. The $a^3\Sigma_u^+$ state, on the other hand, has a deeper well of ~ 1.979 eV. It also has a repulsive barrier, shown in the inset of figure 5.1, at $\sim 5.2a_o$. It is $\sim 6.46 \times 10^{-2}$ eV high. In the $n = 3$ manifold, the ${}^3\Sigma_g^+$ has a well of depth ~ 1.457 eV and a barrier $\sim 6.79 \times 10^{-2}$ eV high at $\sim 4.8a_o$. The ${}^3\Sigma_u^+$ state is purely attractive with a well ~ 2.192 eV deep. All the ${}^3P$ states in the $n = 2$ manifold have repulsive barriers except for the $b^3\Pi_g$ state which is attractive with a well that extends below the $c^3\Sigma_g^+$ minimum.

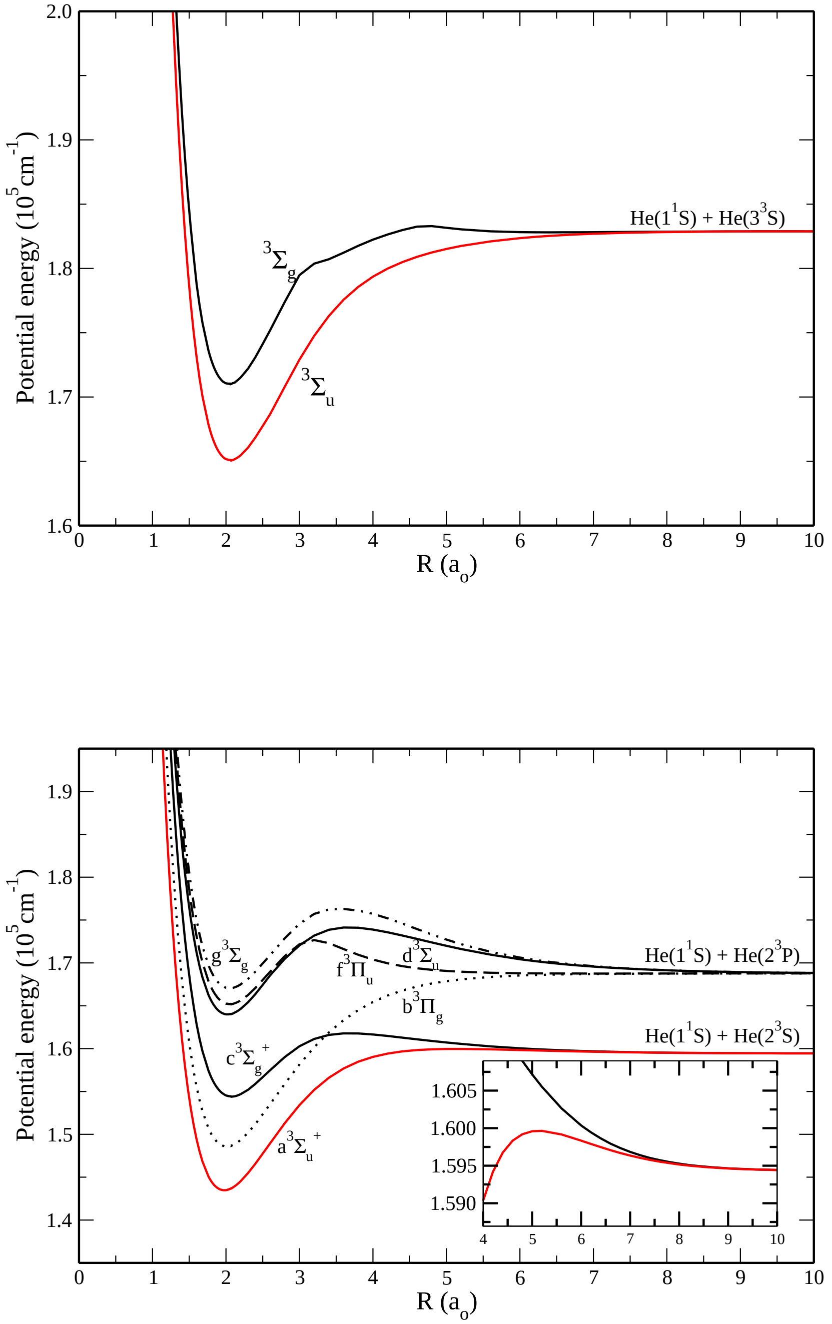

Figure 5.1: Potential energy curves for the interaction of: He(1^1S) with He(3^3S) (top), and He(1^1S) with He(2^3S) and He(2^3P) (bottom). The inset shows the barrier in the $a^3\Sigma_u^+$.

5.3 Cross-sections Results

Single channel scattering calculations were performed using the curves in figure 5.1. The phase shifts obtained were then used to calculate the cross sections according to the formulae given in equations 5.12, 5.13, and 5.14.

The excitation transfer cross section is shown in figure 5.3. It decreases rapidly for energies less than $\sim 500\ cm^{-1}$. As $a^3\Sigma_u^+$ has a barrier with comparable height to this energy at $\sim 5a_o$, the unavailability of enough energy to overcome this barrier suppresses the excitation transfer. In other words, the colliding atoms need a minimum energy to enter the effective region for excitation transfer where the states, $a^3\Sigma_u^+$ and $c^3\Sigma_g^+$, have significant separation. It increases slowly after that with increasing energy.

Figure 5.4 shows the cross section for the diffusion of He(2^3S) atoms in He(1^1S) gas. It results from removing the contributions of small angle scattering from the total elastic cross sections shown in figure 5.2. It has a minimum around $\sim 500\ cm^{-1}$. This is also attributed to the barrier in $a^3\Sigma_u^+$. For larger energies, the diffusion cross section is almost constant. However, it increases as the energy decreases.

Figure 5.2 shows the total elastic cross section. It is dominated by small angle scattering and includes the cross section for the process:

$$He(1^1S) + He^*(1s2s, 2^3S) \to He(1^1S) + He^*(1s2s, 2^3S). \tag{5.15}$$

At very low temperatures, the elastic cross section for $c^3\Sigma_g^+$ approaches a constant while it decreases monotonically to zero for the $a^3\Sigma_u^+$ symmetry. This is consistent with the threshold behavior and with Wigner limit in equation 1.32a. At low temperature, the cross section is dominated by the $l = 0$ term or $s - wave$. This explains the constant limit in the case of $c^3\Sigma_g^+$. For $a^3\Sigma_u^+$, the lowest term is the $l = 1$ or $p - wave$ which causes the cross sections to decrease as E^2. $a^3\Sigma_u^+$ scatters odd partial waves while $c^3\Sigma_g^+$ scatters even partial waves because of symmetry resulting from the two identical nuclei as discussed earlier.

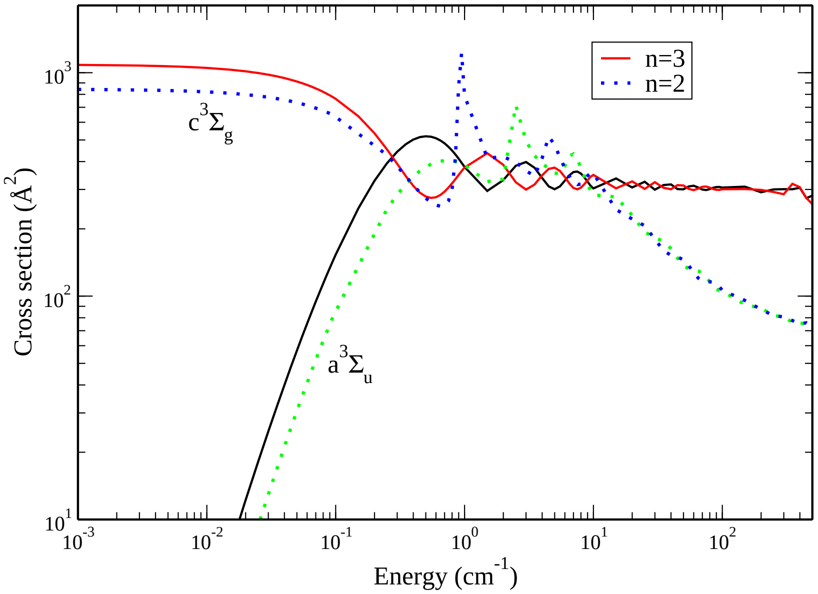

Figure 5.2: Total elastic cross sections for the collision of: He(1^1S) and He(2^3S) atoms (dotted lines), and He(1^1S) and He(3^3S) atoms (solid lines).

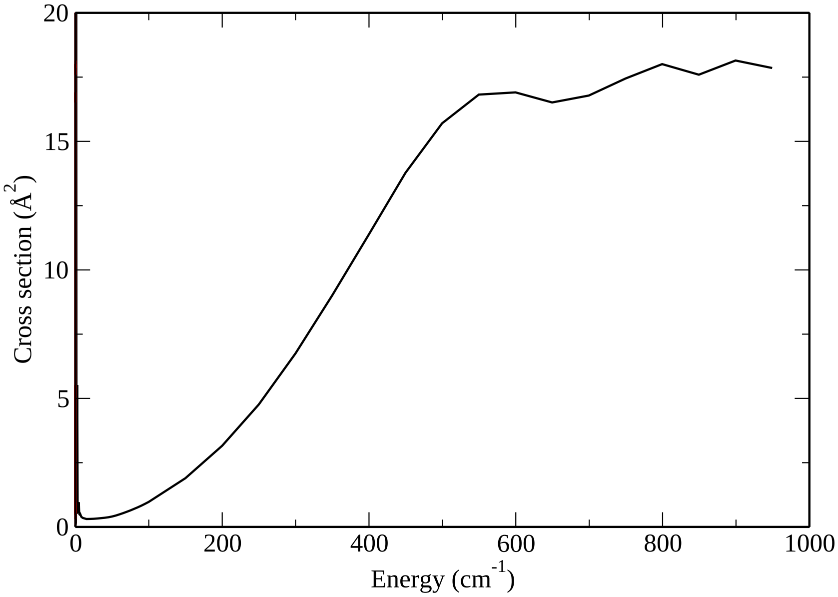

Figure 5.3: Cross section for excitation transfer from the He(2^3S) atoms to the He(1^1S) gas.

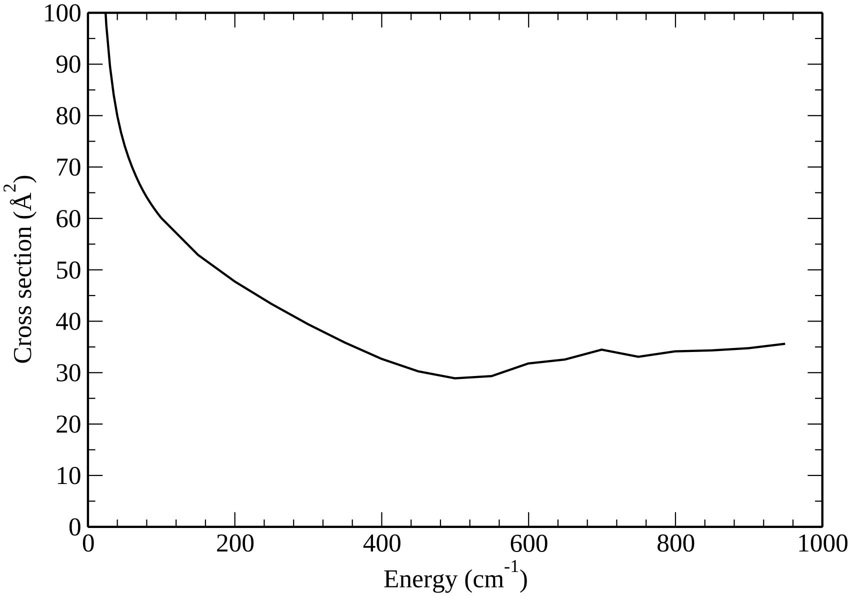

Figure 5.4: Cross section for the diffusion of He(2^3S) atoms in He(1^1S) gas.

Conclusion

New potential energy curves, [88], for the interaction of helium atoms in their ground state with excited helium atoms were used to calculate the cross section for excitation transfer from the He(2^3S) atoms to the He(1^1S) gas, the diffusion of He(2^3S) atoms in He(1^1S) gas, and the total elastic cross sections for the collision of He(1^1S) and He(2^3S) atoms. The results were compared to [91]. A good agreement is observed. Both have the same general features. In both, the diffusion cross section has a minimum at $\sim 500\ cm^{-1}$. Below this energy, the excitation transfer decreases rapidly. The oscillations in the elastic cross section are seen in both results. We have the correct behavior at very low energies where quantum effects, which are sensitive to the long-range interaction, dominate. However, the elastic cross sections for the collision of He(1^1S) and He(2^3S) atoms falls at high energy while it stays almost constant in [91]. The long range interaction is not critical for these energies. The elastic cross sections for the collision of He(1^1S) and He(3^3S) atoms were not calculated before. They display similar features as the potentials of the ${}^3\Sigma_g^+$ and ${}^3\Sigma_u^+$ states have the same general characteristics.

Chapter 6

Conclusions

In the previous chapters, cross sections for different processes were calculated. The procedure, in general, requires the solution of the Schrödinger equation using an interaction potential relevant to the problem to obtain an expression for the cross section. In every case, the starting point is a reliable potential energy surface for the interaction under consideration.

In Chapter 2, the photodissociation of CN

$$\mathrm{CN}(X\ ^2\Sigma^+, v''N'') \quad + \quad h\nu \quad \rightarrow \quad \mathrm{CN}(final\, state, v'N') \quad \rightarrow \quad \mathrm{C} \quad + \quad \mathrm{N}, \tag{6.1}$$

was revisited. The *final state* in the equation above stands for the $^2\Sigma^+(4)$, $^2\Sigma^+(5)$, $^2\Pi(4)$, or $^2\Pi(5)$. Partial and LTE cross sections were evaluated for all rovibrational levels ($v''N''$) of the ground electronic state of CN, X $^2\Sigma^+$, and over a large wavelength range of astrophysical interest. The results will allow for the calculation of reliable CN photodissociation rates for astrophysical environments with varying radiation and dust properties.

The rotational quenching of CO_2 by collisions with He is the subject of Chapters 3 and 4. CO_2 was treated as a rigid rotor in the ground state. If CO_2 is initially in the rotational state specified by the rotational quantum number j_o, transitions of CO_2 represented by:

$$CO_2(j_o) + He \quad \rightarrow \quad CO_2(j') + He, \tag{6.2}$$

were considered. Cross sections for transitions to all possible lower$-j$ rotational states, for a wide range of relative collision energy, were calculated based on the theoretical frame work of [50]. Cross sections for transitions to higher$-j$ rotational states can be obtained through detailed-balance. Cross sections are dominated by the $\mathit{\Delta} j = j' - j = -\mathit{2}$ transition. They follow the exponential energy-gap law [63], and they agree with the Wigner threshold laws [4].

In Chapter 4, the emphasis is on rotational quenching of CO_2 by collisions with He in the ultracold regime. Complex scattering lengths and elastic and inelastic rotational quenching cross sections have been computed for carbon dioxide, with rotational excitation j as high as 200, due to ultracold ^{4}He collisions. It is predicted that the ratio of the elastic to inelastic cross section, or figure-of-merit, is sufficiently large that highly rotationally excited $\mathrm{CO_2}$ could be a viable candidate for cooling and trapping. A novel experiment combining a He buffer gas cell with an optical centrifuge is proposed as a means of producing rotationally hot, but translationally cold $\mathrm{CO_2}$. A high-flux beam of cold $\mathrm{CO_2}$ super rotors could be created and used for a variety of scattering experiments.

The interaction of two helium atoms according to

$$He(1^1S) + He^*(1s2s, 2^3S) \rightarrow He^*(1s2s, 2^3S) + He(1^1S), \tag{6.3}$$

was considered in Chapter 5. In this case, the fact that the two interacting nuclei are identical must be taken into account. New potential energy curves, [88], were used to calculate the cross section for excitation transfer from the He(2^3S) atoms to the He(1^1S) gas, the diffusion of He(2^3S) atoms in He(1^1S) gas, and the total elastic cross sections for the collision of He(1^1S) and He(2^3S) atoms. The results were compared to [91]. A good agreement is observed. The elastic cross sections for the collision of He(1^1S) and He(3^3S) were calculated. They were not calculated before.

References

[1] H. Lavendy, J. M. Robbe, and G. Gandara, "Theoretical photodissociation probability of the CN radical," *J. Phys. B: At. Mol. Phys.*, vol. 20, p. 3067, 1987.

[2] M. Weissbluth, *Atoms and Molecules.* San Diego, USA: Academic Press, 1978.

[3] M. S. Child, *Molecular Collision Theory.* Theoretical Chemistry, London, UK: Academic Press, 1974.

[4] E. P. Wigner, "On the behavior of cross sections near thresholds," *Phys. Rev.*, vol. 73, pp. 1002–1009, May 1948.

[5] R. Schinke, *Photodissociation Dynamics.* Cambridge Monographs on Atomic, Molecular, and Chemical Physics 1, Cambridge, UK: Cambridge University Press, 1993.

[6] J. V. V. Kasper and G. C. Pimentel, "Atomic iodine photodissociattion laser," *Appl. Phys. Lett.*, vol. 5, p. 231, 1964.

[7] K. P. Kirby and E. F. van Dishoeck, "Photodissociation processes in diatomic molecules of astrophysical interest," in *Advances in atomic and molecular physics* (Sir D. Bates and B. Bederson, eds.), vol. 25, p. 437, USA: Academic Press INC., 1988.

[8] T. P. Snow and B. J. McCall, "Diffuse atomic and molecular clouds," *Annu. Rev. Astron. Astrophys.*, vol. 44, pp. 367–414, 2006.

[9] D. J. Hollenbach and A. G. G. M. Tielens, "Dense photodissociation regions (pdrs)," *Annu. Rev. Astron. Astrophys.*, vol. 35, pp. 179–215, September 1997.

[10] E. F. van Dishoeck, B. Jonkheid, and M. C. van Hemert, "Photoprocesses in protoplanetary disks," *Faraday Discuss.*, vol. 133, pp. 231–243, 2006.

[11] E. Herbst and E. F. van Dishoeck, "Complex organic interstellar molecules," *Annu. Rev. Astron. Astrophys.*, vol. 47, pp. 427–480, 2009.

[12] I. W. M. Smith, "Laboratory astrochemistry: Gas-phase processes," *Annu. Rev. Astron. Astrophys.*, vol. 49, pp. 29–66, 2011.

[13] A. McKellar, "Evidence for the molecular origin of some hitherto unidentified interstellar lines," *Publ. Astron. Soc. Pac.*, vol. 52, p. 187, 1940.

[14] P. Thaddeus, "The Short-Wavelength Spectrum of the Microwave Background," *Annu. Rev. Astron. Astrophys.*, vol. 10, p. 305, 1972.

[15] R. H. Dicke, P. J. E. Peebles, P. G. Roll, and D. T. Wilkinson, "Cosmic Black-Body Radiation.," *Astrophys. J.*, vol. 142, pp. 414–419, July 1965.

[16] A. A. Penzias and R. W. Wilson, "A Measurement of Excess Antenna Temperature at 4080 Mc/s.," *Astrophys. J.*, vol. 142, pp. 419–421, July 1965.

[17] A. A. Penzias and R. W. Wilson, "Measurement of the Flux Density of CAS a at 4080 Mc/s.," *Astrophys. J.*, vol. 142, p. 1149, Oct. 1965.

[18] A. A. Penzias and R. W. Wilson, "Determination of the Microwave Spectrum of Galactic Radiation," *Astrophys. J.*, vol. 146, p. 666, Dec. 1966.

[19] E. F. van Dishoeck and J. H. Black, "Interstellar C_2, CH, and CN in translucent molecular clouds," *Astrophys. J.*, vol. 340, pp. 273–297, 1989.

[20] S. Miyake, C. D. Gay, and P. C. Stancil, "Rovibrationally resolved photodissociation of HeH^+," *Astrophys. J.*, vol. 735, p. 21, July 2011.

[21] E. E. Whiting and R. W. Nicholls, "Reinvestigation of rotational-line intensity factors in diatomic spectra," *Astrophys. J. Supp.*, vol. 27, p. 1, 1974.

[22] J. W. Cooley, "An improved eigenvalue corrector formula for solving the schrodinger equation for central fields," *Mathematics of Computation*, vol. 15, p. 363, October 1961.

[23] D. Cvetko, A. Lausi, A. Morgante, F. Tommasini, P. Cortona, and M. G. Dondi, "A new model for atom-atom potentials," *J. Chem. Phys.*, vol. 100, p. 2052, 1994.

[24] A. Dalgarno and A. L. Stewart, "A perturbation calculation of properties of the 1sσ and 2pσ states of HeH^{2+}," *Proc. Roy. Soc. (London)*, vol. A238, p. 276, 1956.

[25] T. Y. Chang, "Moderately long-range interatomic forces," *Rev. Mod. Phys.*, vol. 39, p. 911, 1967.

[26] I. Borges Jr., P. J. S. B. Caridade, and A. J. C. Varandas, "Potential energy curves for $X^1\Sigma^+$ and $A^1\Pi$ states of CO: The $A^1\Pi$ (v'=123) $\rightarrow$ $X^1\Sigma^+$ (v"=0,1) transitions," *J. Mol. Spectrosc.*, vol. 209, pp. 24–29, September 2001.

[27] J. Le Bourlot and E. Roueff, "Intercombination transitions between levels $X^1\Sigma_g^+$ and $a^3\Pi_u$ in C_2," *J. Mol. Spectrosc.*, vol. 120, p. 157, 1986.

[28] K. P. Huber and G. Herzberg, *Constants of Diatomic Molecules.* Molecular Spectra and Molecular Structure IV, Princeton, USA: Van Nostrand Reinhold, 1979.

[29] Y. Ralchenko, A. E. Kramida, J. Reader, and NIST ASD Team. NIST Atomic Spectra Database (version 4.0) [Online]. Available: `http://physics.nist.gov/asd`, 2010.

[30] J. Woodall, M. Agndez, A. J. Markwick-Kemper, and T. J. Millar, “The umist database for astrochemistry 2006,” *A & A*, vol. 466, p. 1197, 2007.

[31] E. F. van Dishoeck, “Photodissociation and photoionization processes,” in *Rate Coefficients in Astrochemistry* (T. J. Millar and D. A. Williams, eds.), vol. 146 of *Astrophysics and Space Science Library*, pp. 49–72, 1988.

[32] W. G. Roberge, D. Jones, S. Lepp, and A. Dalgarno, “Interstellar photodissociation and photoionization rates,” *Astrophys. J. Supp.*, vol. 77, pp. 287–297, Oct. 1991.

[33] J. S. Mathis, W. Rumpl, and K. H. Nordsieck, “The size distribution of interstellar grains,” *Astrophys. J.*, vol. 217, pp. 425–433, Oct. 1977.

[34] B. T. Draine and H. M. Lee, “Optical properties of interstellar graphite and silicate grains,” *Astrophys. J.*, vol. 285, pp. 89–108, Oct. 1984.

[35] D. Calzetti, “The dust opacity of star-forming galaxies,” *Publications of the Astronomical Society of the Pacific*, vol. 113, pp. 1449–1485, 2001.

[36] U. J. Sofia, J. T. Lauroesch, D. M. Meyer, and S. I. B. Cartledge, “Interstellar Carbon in Translucent Sight Lines,” *Astrophys. J.*, vol. 605, pp. 272–277, Apr. 2004.

[37] D. E. Welty, S. R. Federman, R. Gredel, J. A. Thorburn, and D. L. Lambert, “VLT UVES Observations of Interstellar Molecules and Diffuse Bands in the Magellanic Clouds,” *Astrophys. J. Supp.*, vol. 165, pp. 138–172, July 2006.

[38] T. Dunham, Jr., “Interstellar neutral potassium and neutral calcium,” *Publications of the Astronomical Society of the Pacific*, vol. 49, pp. 26–28, February 1937.

[39] A. Fuente, S. García-Burillo, M. Gerin, D. Teyssier, A. Usero, J. R. Rizzo, and P. de Vicente, “Photon-dominated Chemistry in the Nucleus of M82: Widespread HOC^+ Emission in the Inner 650 Parsec Disk,” *Astrophys. J.*, vol. 619, pp. L155–L158, Feb. 2005.

[40] I. Cherchneff, A. E. Glassgold, and G. A. Mamon, “The formation of cyanopolyyne molecules in IRC + 10216,” *Astrophys. J.*, vol. 410, pp. 188–201, June 1993.

[41] S. D. Doty and C. M. Leung, “Detailed Chemical Modeling of the Circumstellar Envelopes of Carbon Stars: Application to IRC +10216,” *Astrophys. J.*, vol. 502, p. 898, Aug. 1998.

[42] C. Walsh, H. Nomura, T. J. Millar, and Y. Aikawa, “Chemical Processes in Protoplanetary Disks. II. On the Importance of Photochemistry and X-Ray Ionization,” *Astrophys. J.*, vol. 747, p. 114, Mar. 2012.

[43] V. V. Akimkin, Y. N. Pavlyuchenkov, A. I. Vasyunin, D. S. Wiebe, M. S. Kirsanova, and T. Henning, “Uv-controlled physical and chemical structure of protoplannetary disks,” *Astrophys. Space Sci.*, vol. 335, pp. 33–38, 2011.

[44] C. Walsh, T. J. Millar, and H. Nomura, “Chemical Processes in Protoplanetary Disks,” *Astrophys. J.*, vol. 722, pp. 1607–1623, Oct. 2010.

[45] L. B. d’Hendecourt and M. J. de Muizon, “The discovery of interstellar carbon dioxide,” *Astron. Astrophys.*, vol. 223, pp. L5–L8, 1989.

[46] T. de Graauw, D. C. B. Whittet, P. A. Gerakines, O. H. Bauer, D. A. Beintema, A. C. A. Boogert, D. R. Boxhoorn, J. E. Chiar, P. Ehrenfreund, H. Feuchtgruber, F. P. Helmich, A. M. Heras, R. Huygen, D. J. M. Kester, D. Kunze, F. Lahuis, K. J. Leech, D. Lutz, P. W. Morris, T. Prusti, P. R. Roelfsema, A. Salama, S. G. Schaeidt, W. A. Schutte, H. W. W. Spoon, A. G. G. M. Tielens, E. A. Valentijn, B. Vandenbusshe, E. F. van Dishoeck, P. R. Wesselius, E. Wieprecht, and C. M. Wright, “SWS observations of solid CO_2 in molecular clouds.,” *Astron. Astrophys.*, vol. 315, pp. L345–L348, Nov. 1996.

[47] E. F. van Dishoeck, F. P. Helmich, T. de Graauw, J. H. Black, A. C. A. Boogert, P. Ehrenfreund, P. A. Gerakines, J. H. Lacy, T. J. Millar, W. A. Schutte, A. G. G. M. Tielens, D. C. B. Whittet, D. R. Boxhoorn, D. J. M. Kester, K. Leech, P. R. Roelfsema, A. Salama, and B. Vandenbussche, “A search for interstellar gas-phase CO_2. Gas: solid state abundance ratios.,” *Astron. Astrophys.*, vol. 315, pp. L349–L352, Nov. 1996.

[48] S. Green and P. Thaddeus, “Rotational excitation of CO by collisions with He, H, and H_2 under conditions in interstellar clouds,” *Astrophys. J.*, vol. 205, pp. 766–785, 1976.

[49] S. Green and P. Thaddeus, “Rotational excitation of HCN by collisions,” *Astrophys. J.*, vol. 191, pp. 653–657, 1974.

[50] A. M. Arthurs and A. Dalgarno, “The Theory of Scattering by a Rigid Rotor,” in *Proceedings of the Royal Society A: Mathematical, Physical and Engineering Sciences*, vol. 256, (London, UK), pp. 540–551, The Royal Society, 1960.

[51] N. F. Mott and H. S. W. Massey, *The Theory of Atomic Collisions.* The International Series of Monographs on Physics 35, Oxford, UK: Oxford University Press, third ed., 1965.

[52] J. N. Murrell and S. D. Bosanac, *Introduction to the Theory of Atomic and Molecular Collisions.* England: John Wiley and Sons, 1989.

[53] D. Flower, *Molecular Collisions in the Interstellar Medium.* Cambridge Astrophysics Series 42, Cambridge, UK: Cambridge University Press, second ed., 2007.

[54] R. B. Bernstein, ed., *Atom-Molecule Collision Theory: A Guide for the Experimentalist.* New York, USA: Plenum Press, 1979.

[55] I. C. Percival and M. J. Seaton, “The Partial Wave Theory of Electron-Hydrogen Atom Collisions,” in *Mathematical Proceedings of the Cambridge Philosophical Society*, vol. 53, (Cambridge, UK), pp. 654–662, Cambridge University Press, 1957.

[56] C. F. Curtiss and F. T. Adler, "The scattering of atoms from diatomic molecules," *J. Chem. Phys.*, vol. 20, p. 249, 1952.

[57] R. T. Pack, "Space-fixed vs. body-fixed axes in atom-diatomic molecule scattering. sudden approximations," *J. Chem. Phys.*, vol. 60, p. 633, 1974.

[58] H. Ran and D. Xie, "A new potential energy surface and predicted infrared spectra of He-CO_2: Dependence on the antisymmetric stretch of CO_2," *J. Chem. Phys.*, vol. 128, p. 124323, March 2008.

[59] J. M. Hutson and S. Green, "MOLSCAT computer code, version 14." distributed by Collaborative Computational Project No. 6 of the Engineering and Physical Sciences Research Council. Daresbury Laboratory, UK, 1994.

[60] M. H. Alexander and D. E. Manolopoulos, "A stable linear reference potential algorithm for solution of the quantum close-coupled equations in molecular scattering theory," *J. Chem. Phys.*, vol. 86, p. 2044, February 1987.

[61] D. E. Manolopoulos, "An improved log derivative method for inelastic scattering," *J. Chem. Phys.*, vol. 85, p. 6425, 1986.

[62] B. R. Johnson, "Multichannel log-derivative method for scattering calculations," *J. Comput. Phys.*, vol. 13, pp. 445–449, 1973.

[63] J. C. Polanyi and K. B. Woodall, "Mechanism of rotational relaxation," *J. Chem. Phys.*, vol. 56, p. 1563, February 1972.

[64] B. Yang and P. C. Stancil, "Rotational quenching of CO_2 by collision with he atoms," *J. Chem. Phys.*, vol. 130, p. 134319, April 2009.

[65] J. Doyle, B. Friedrich, R. V. Krems, and F. Masnou-Seeuws, "Quo vadis, cold molecules?," *Eur. Phys. J. D*, vol. 31, pp. 149–164, 2004.

[66] R. V. Krems, "Molecules near absolute zero and external field control of atomic and molecular dynamics," *Int. Rev. Phys. Chem.*, vol. 24, p. 99, 2005.

[67] P. F. Weck and N. Balakrishnan, "Importance of long-range interactions in chemical reactions at cold and ultracold temperatures," *Int. Rev. Phys. Chem.*, vol. 25, p. 283, 2006.

[68] G. Quéméner, N. Balakrishnan, and A. Dalgarno, "Inelastic collisions and chemical reactions of molecules at ultracold temperatures," in *Cold Molecules: Theory, Experiment, Application* (R. V. Krems, W. C. Stwalley, and B. Friedrich, eds.), p. 69, USA: CRC Press, 2009.

[69] L. D. Carr, D. DeMille, R. V. Krems, and J. Ye, "Cold and ultracold molecules: science, technology and applications," *New J. Phys.*, vol. 11, p. 055049, May 2009.

[70] O. Dulieu and C. Gabbanini, "The formation and interactions of cold and ultracold molecules: new challenges for interdisciplinary physics," *Rep. Prog. Phys.*, vol. 72, p. 086401, August 2009.

[71] J. D. Weinstein, R. deCarvalho, T. Guillet, B. Friedrich, and J. M. Doyle, "Magnetic trapping of calcium monohydride molecules at millikelvin temperatures," *Nature (London)*, vol. 395, p. 148, September 1998.

[72] J. Karczmarek, J. Wright, P. Corkum, and M. Ivanov, "Optical centrifuge for molecules," *Phys. Rev. Lett.*, vol. 82, pp. 3420–3423, 1999.

[73] J. Li, J. T. Bahns, and W. C. Stwalley, "Scheme for state-selective formation of highly rotationally excited diatomic molecules," *J. Chem. Phys.*, vol. 112, p. 6255, April 2000.

[74] D. M. Villeneuve, S. A. Aseyev, P. Dietrich, M. Spanner, M. Y. Ivanov, and P. B. Corkum, "Forced molecular rotation in an optical centrifuge," *Phys. Rev. Lett.*, vol. 85, p. 542, July 2000.

[75] R. C. Forrey, "Cooling and trapping of molecules in highly excited rotatinal states," *Phys. Rev. A*, vol. 63, p. 051403(R), May 2001.

[76] R. C. Forrey, "Prospects for cooling and trapping rotationally hot molecules," *Phys. Rev. A*, vol. 66, p. 023411, August 2002.

[77] L. D. Landau and E. M. Lifshitz, *Quantum Mechanics.* Oxford, UK: Pergamon Press, 1977.

[78] N. Balakrishnan, V. Kharchenko, R. C. Forrey, and A. Dalgarno, "Complex scattering lengths in multi-channel atom-molecule collisions," *Chem. Phys. Lett.*, vol. 280, pp. 5–9, November 1997.

[79] B. Yang, R. C. Forrey, P. C. Stancil, and N. Balakrishnan, "Complex scattering lengths for ultracold He collisions with rotationally excited linear and nonlinear molecules," *Phys. Rev. A*, vol. 82, p. 052711, November 2010.

[80] D. Villeneuve. Private Communication, 2001.

[81] L. Yuan, J. Du, and A. S. Mullin, "Energy-dependence dynamics of large -ΔE collisions: Highly vibrationally excited azulene (E=20390 and 38580 cm^{-1}) with CO$_2$," *J. Chem. Phys.*, vol. 129, p. 014303, July 2008.

[82] A. S. Mullin and et al. Bull. Am. Phys. Soc., 2009.

[83] S. E. Maxwell, N. Brahms, R. deCarvalho, D. R. Glenn, J. S. Helton, S. V. Nguyen, D. Patterson, J. Petricka, D. DeMille, and J. M. Doyle, "High-flux beam source for cold, slow atoms or molecules," *Phys. Rev. Lett.*, vol. 95, p. 173201, October 2005.

[84] H. S. W. Massey and R. A. Smith, “The Passage of Positive Ions Through Gases,” in *Proceedings of the Royal Society A: Mathematical, Physical and Engineering Sciences*, vol. 142, (London, UK), pp. 142–172, The Royal Society, 1933.

[85] R. A. Buckingham and A. Dalgarno, “The interaction of normal and metastable helium atoms,” in *Proceedings of the Royal Society A: Mathematical, Physical and Engineering Sciences*, vol. 213, (London, UK), p. 327, The Royal Society, July 1952.

[86] R. A. Buckingham and A. Dalgarno, “Diffusion and excitation transfer of metastable helium in normal gaseous helium,” in *Proceedings of the Royal Society A: Mathematical, Physical and Engineering Sciences*, vol. 213, (London, UK), p. 506, The Royal Society, July 1952.

[87] S. Geltman, *Topics in Atomic Collision Theory.* Pure and Applied Physics 30, New York and London: Academic Press, INC., 1969.

[88] R. Buenker. Private Communication, 2012.

[89] R. J. Buenker and S. D. Peyerimhoff, “Individualized configuration selection in ci calculations with subsequent energy extrapolation,” *Theoretica Chimica Acta ‘Theoretical Chemistry Accounts’*, vol. 35, pp. 33–58, 1974.

[90] S. Krebs and R. J. Buenker, “A new table-direct configuration interaction method for the evaluation of hamiltnian matrix elements in a basis of linear combination of spin-adapted functions,” *J. Chem. Phys.*, vol. 103, p. 5613, 1995.

[91] D. Vrinceanu and H. R. Sadeghpour, “He(1^1S)-He(2^3S) collision and radiative transition at low temperatures,” *Phys. Rev. A*, vol. 65, p. 062712, June 2002.